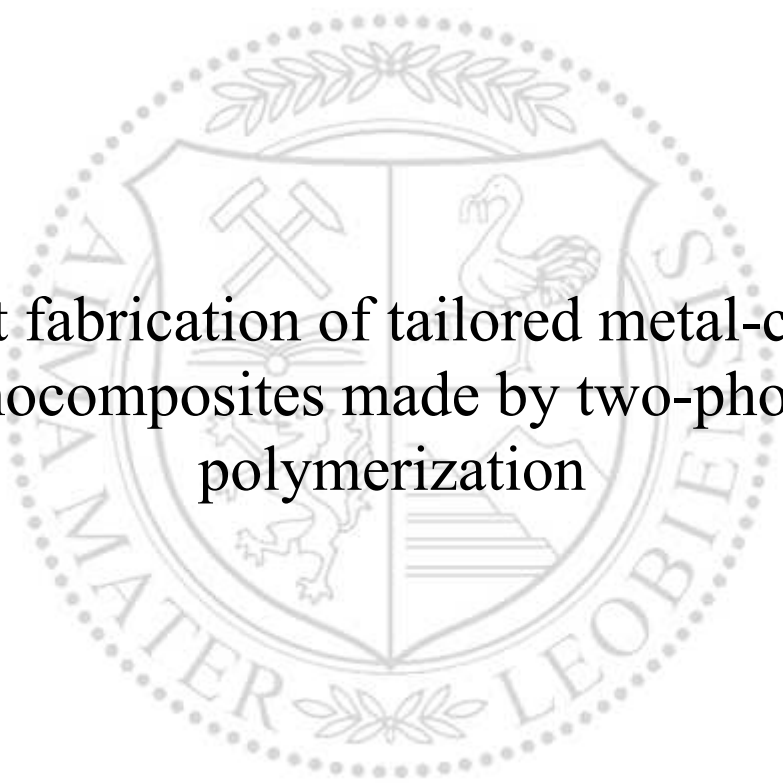




Chair of Materials Physics

Master's Thesis



Direct fabrication of tailored metal-carbon  
nanocomposites made by two-photon  
polymerization

Marco Paul Jahn, BSc

May 2024





**EIDESSTATTLICHE ERKLÄRUNG**

Ich erkläre an Eides statt, dass ich diese Arbeit selbstständig verfasst, andere als die angegebenen Quellen und Hilfsmittel nicht benutzt, den Einsatz von generativen Methoden und Modellen der künstlichen Intelligenz vollständig und wahrheitsgetreu ausgewiesen habe, und mich auch sonst keiner unerlaubten Hilfsmittel bedient habe.

Ich erkläre, dass ich den Satzungsteil „Gute wissenschaftliche Praxis“ der Montanuniversität Leoben gelesen, verstanden und befolgt habe.

Weiters erkläre ich, dass die elektronische und gedruckte Version der eingereichten wissenschaftlichen Abschlussarbeit formal und inhaltlich identisch sind.

Datum 06.05.2024

---

Unterschrift Verfasser/in  
Marco Paul Jahn



## Acknowledgements

I would like to express my deepest gratitude to my supervisors Dr. Christoph Gammer as well as Professor Jürgen Eckert, the director of the chair of material physics of the Montanuniversität Leoben, without whom this work would not have been possible.

I am also extremely grateful for the work of Dr. Alice Lassnig, who trained me on the coating system and also operated the FIB and TEM.

Furthermore, I would like to thank Dr. Stefan Wurster for training me on the vacuum furnace and the SEM, as well as DI Alexander Jelinek for interesting discussions about the NanoScribe printer.

Finally, I would like to mention my family, who has supported me over all these years in my studies of materials science.

# Contents

<b>Abstract</b>	<b>1</b>
<b>Kurzfassung</b>	<b>2</b>
<b>List of Abbreviations</b>	<b>3</b>
<b>List of Figures</b>	<b>4</b>
<b>List of Tables</b>	<b>6</b>
<b>1 Introduction</b>	<b>7</b>
<b>2 Fundamentals</b>	<b>9</b>
2.1 Direct Laser Writing . . . . .	9
2.1.1 Two-Photon Absorption . . . . .	10
2.1.2 Two-Photon Polymerization . . . . .	12
2.2 Pyrolysis . . . . .	13
2.3 PVD - Magnetron sputtering . . . . .	15
2.4 Focused Ion Beam milling . . . . .	18
2.5 In situ transmission electron microscopy . . . . .	19
<b>3 Experimental procedure</b>	<b>21</b>
3.1 Fabrication of nanoscale deformation structures . . . . .	22
3.2 Comparison of different pyrolysis temperatures . . . . .	24
3.3 Design optimization for isotropic shrinkage . . . . .	29
3.3.1 Final sample design . . . . .	32
3.4 Coating procedure . . . . .	34
3.4.1 Filling grade depending on the sample geometry . . . . .	35
3.5 Workflow . . . . .	37

<b>4</b>	<b>Results and discussion</b>	<b>38</b>
4.1	Results of the nanoscale deformation structures . . . . .	38
4.2	Evaluation of the pyrolysis experiments . . . . .	41
4.3	Filling grade in dependence of the sample geometry . . . . .	43
4.4	Detailed TEM investigation of the tailored metal-carbon nanocomposites . . . . .	44
4.5	In situ deformation of the tailored metal-carbon nanocomposites in the TEM . . . . .	49
<b>5</b>	<b>Conclusion and outlook</b>	<b>51</b>
<b>6</b>	<b>Appendix</b>	<b>53</b>
	<b>References</b>	<b>54</b>

## Abstract

Additive manufacturing, also widely referred to as 3D printing, is an emerging and innovative manufacturing process that differs fundamentally from conventional manufacturing processes. In research and industry, it opens up completely new possibilities for scientists. 3D printing using two-photon polymerization is one of the photopolymerization processes, whereby extremely small components can be produced. In this work, two-photon polymerization is used to produce nanoscale deformation structures as well as nanocomposite materials.

The deformation structures show very good deformation behavior and offer the possibility of testing a large number of samples in a short time. Other processes, such as pyrolysis, were used in the successful production of composite materials. The work shows that two-photon polymerization is an ideal tool for producing defined model systems.



## Kurzfassung

Additive Fertigung, weitgehend auch als 3D-Druck bezeichnet, ist ein aufstrebendes und innovatives Fertigungsverfahren, welches sich grundlegend von konventionellen Herstellungsprozessen unterscheidet. In der Forschung und Industrie verhilft es Wissenschaftlerinnen und Wissenschaftlern zu völlig neuen Möglichkeiten. Der 3D-Druck mittels Zwei-Photonen-Polymerisation gehört zu den Verfahren der Photopolymerisation, wobei extrem kleine Bauteile realisiert werden können. In dieser Arbeit werden mittels Zwei-Photonen-Polymerisation zum einen nanoskalige Verformungsstrukturen als auch Nanokompositwerkstoffe hergestellt.

Die Verformungsstrukturen zeigen ein sehr gutes Deformationsverhalten und bieten die Möglichkeit, ein hohes Kontingent an Proben in kurzer Zeit zu prüfen. Bei der erfolgreichen Herstellung von Kompositwerkstoffen wurden weitere Verfahren, wie etwa die Pyrolyse, herangezogen. Die Arbeit zeigt, dass die Zwei-Photonen-Polymerisation ein ideales Werkzeug zur Herstellung definierter Modellsysteme ist.

## List of Abbreviations

1PA	One-photon absorption
2PA	Two-photon absorption
2PP	Two-photon polymerization
C	Carbon
CAD	Computer aided design
Cu	Copper
DLW	Direct Laser Writing
EDS	Energy dispersive spectroscopy
FIB	Focused ion beam
Ga	Gallium
LMIS	Liquid metal ion source
MEMS	Micro-electro-mechanical Systems
Pt	Platinum
PTP	Push-to-pull
PVD	Physical vapor deposition
SEM	Scanning electron microscope
TEM	Transmission electron microscope
TGA	Thermogravimetric analysis

## List of Figures

1	Size comparison of a MEMS testing device . . . . .	7
2	Schematic illustration of the DLW process . . . . .	9
3	Illustration of the comparison between 1PA and 2PA . . . . .	11
4	Energy band model for 1PA and 2PA . . . . .	12
5	Distribution of intensity . . . . .	13
6	Process flow of pyrolysed carbon fabrication . . . . .	14
7	Pyrolysis of IP-Dip . . . . .	15
8	Overview of the major PVD techniques . . . . .	16
9	Schematic setup of a magnetron sputtering device . . . . .	17
10	Anders structure zone diagram . . . . .	17
11	Setup of a dual-beam platform (FIB-SEM) . . . . .	18
12	Comparison of different ion species . . . . .	19
13	Overview of in situ factors and applications . . . . .	20
14	Photonic Professional GT2 . . . . .	21
15	Small feature solution set . . . . .	21
16	CAD model of the PTP device . . . . .	22
17	PTP device in DeScribe . . . . .	23
18	PTP device imaged in the TEM . . . . .	23
19	CAD model of the test geometries . . . . .	24
20	Spiral constructed in DeScribe . . . . .	25
21	Combination of the test geometries and the spirals . . . . .	25
22	Temperature profile . . . . .	26
23	SEM images show shrinkage . . . . .	27
24	Statue of Liberty at different pyrolysis temperatures . . . . .	28
25	Test structure on pillars . . . . .	30
26	Test structure on spirals . . . . .	30
27	Test structure on pillars after pyrolysis . . . . .	30

*LIST OF FIGURES*

---

28	Test structure on spirals after pyrolysis . . . . .	30
29	Test structure on pillars imaged at 30° angle . . . . .	30
30	Test structure on spirals imaged at 30° angle . . . . .	30
31	DeScribe model of a test structure on a rhombic cuboctahedron	31
32	Test structure on a rhombic cuboctahedron after pyrolysis . . .	32
33	DeScribe model of the final structure . . . . .	33
34	Final structure after pyrolysis at 450°C . . . . .	34
35	Thin Film Deposition System . . . . .	34
36	Targets during deposition process . . . . .	34
37	SEM images for comparison before and after coating . . . . .	35
38	SEM images of completely and partially filled structures . . .	36
39	Workflow chart from 3D printing to testing . . . . .	37
40	Nanoscale deformation structure before and after failure . . .	38
41	Raw load-displacement curve . . . . .	39
42	BF-STEM images of the fractured sample . . . . .	40
43	Boltzmann fit of the pyrolysed samples . . . . .	42
44	Filling grade depending on the gap to height aspect ratio . . .	43
45	Final specimen coated with 1 µm of copper . . . . .	45
46	Top view with first three cuts . . . . .	46
47	Mounting of the nanomanipulator . . . . .	46
48	Transfer of the sample to the specimen holder . . . . .	46
49	Attached sample . . . . .	47
50	Begin of the thinning process . . . . .	47
51	Sample with final thickness . . . . .	47
52	Final sample imaged in the TEM . . . . .	48
53	Cu-C nanocomposite mounted for in situ in the TEM . . . . .	49
54	Slow crack propagation . . . . .	50
55	TGA analysis of polymerised IP-Dip . . . . .	53

## List of Tables

1	Parameters for magnetron sputtering . . . . .	35
2	Results of the Boltzmann fit . . . . .	42
3	Properties of IP-Dip . . . . .	53

# 1 Introduction

The miniaturisation of components places greater and more precise demands on the manufacturing process. Added to this is the need to individually adapt these parts to the system required later. The design of microsystems such as MEMS (see Figure 1), for example, often proves to be complex. This is where the young technology of two-photon polymerization comes into play. It has its origins in multi-photon fluorescence microscopy [1] and was developed in 1997 by Shoji Maruo, Osamu Nakamura and Satoshi Kawata at the University of Osaka [2]. The process, also known as direct laser writing, shows great potential in the production of microsystems, as it is possible to realize any three-dimensional structures in the micrometer and submicrometer range.

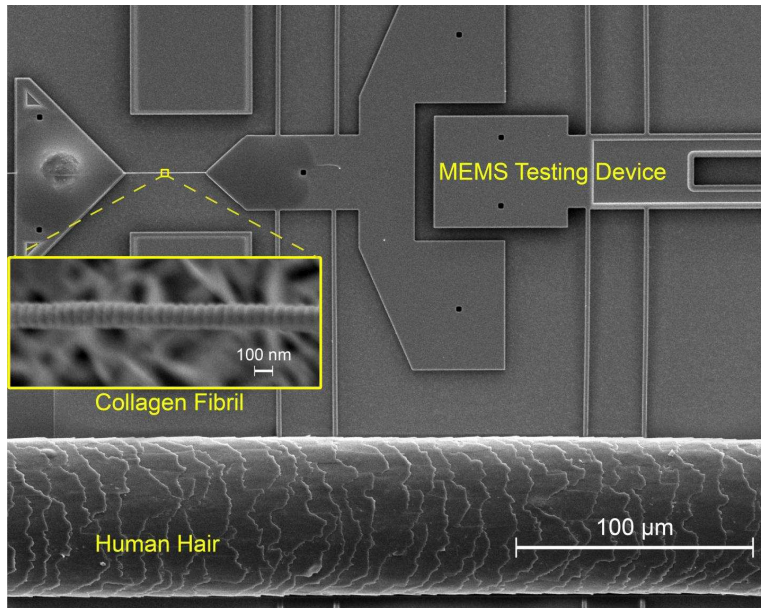


Figure 1: Size comparison of a MEMS testing device and a human hair [3]

The direct laser writing workflow is relatively simple. First, the desired structures are designed in a CAD software, then exported in STL format and then loaded into the 3D printer. A laser now writes the pattern onto a photosensi-

tive resist and illuminates individual areas. A photochemical reaction takes place in these zones, whereby the resin polymerizes and the component is created step by step. The aim of this work is to create nanoscale deformation structures and nanocompound materials using two-photon polymerization. This shows that an almost limitless combination of materials, component size and the shape of the test specimen exists and can also be produced.

## 2 Fundamentals

The core of this work is to fabricate tailored nanoscale structures using two-photon polymerization. Therefore, this chapter discusses all the underlying physical principles on which the experiments are based. First, the basics of direct laser writing, *i.e.* the printing process, are discussed. This is followed by an overview of the processes during pyrolysis and the coating procedure. For the sake of completeness, FIB (*Focused ion beam*) and the TEM (*Transmission electron microscope*) are also explained in a brief summary.

### 2.1 Direct Laser Writing

In simple terms, direct laser writing is a process with which free-standing 3-dimensional structures can be created in just one step. A focused laser beam is guided through a negative photoresist based on a pre-programmed pattern, whereby certain areas are illuminated and thus polymerised. After developing in solvents, only the polymerised areas remain and thus a free-standing three-dimensional structure remains.

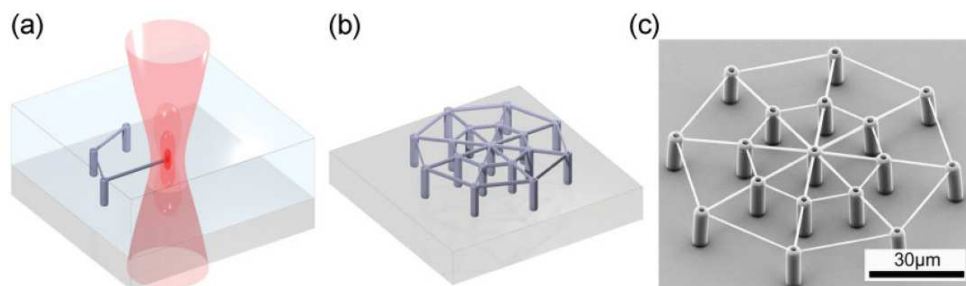


Figure 2: Schematic illustration of the DLW process [4]. a) A photoresist is illuminated by a focused laser beam. b) After cleaning the sample, the polymerized regions remains as a free standing structure. c) Final SEM image of the structure.



The DLW offers a wide range of applications and has already been successfully implemented in various areas [5]. To name just a few examples: MEMS [6, 7], photonic crystals [8, 9], biomedical applications [10, 11] and microlenses [12, 13].

In order to understand how DLW works, the fundamentals of the physical phenomena on which the process is based must be clarified. In this case it is the so called 2 photon absorption (*2PA*) and in a broader sense the 2 photon polymerization (*2PP*). These will be explained below and finally materials used in these processes will be discussed.

### 2.1.1 Two-Photon Absorption

In 1931, Maria Göppert-Mayer was the first to describe the phenomenon of two-photon absorption in her dissertation [14]. It was not until 30 years later, shortly after the invention of the laser, that her theory of 2PA was proven by Kaiser and Garrett [15].

To clarify why DLW is based on 2 photon absorption and not on 1 photon absorption, the principles are explained and compared. Due to the scope of the 2PA and the complexity of this topic, only the points relevant to this work are discussed below.

If an atom or molecule is transferred from the ground state to an excited state by absorbing a single photon, this is referred to as 1PA (compare Figure 4). The probability of absorbing the photon is proportional to the probability of finding a photon near the atom or molecule. Therefore, the absorption probability is also proportional to the photon density and subsequently to the light intensity, which is described by Formula 1 [16].

$$P_{1PA} \propto I \quad (1)$$

Therefore, all photons in the light cone are absorbed, which leads to polymerization of the entire area. This linear absorption behavior is shown in Figure 3 on the left.

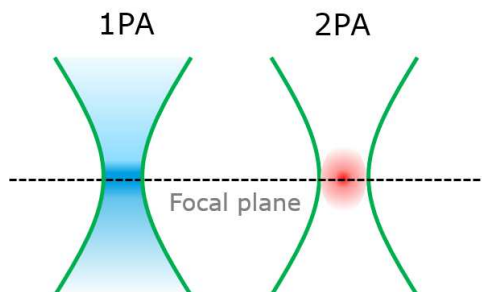


Figure 3: Illustration of the comparison between 1PA and 2PA. [17]

In the 2PA, not just one photon but two photons are absorbed simultaneously. The absorption probability can be expressed by Equation 2 [16].

$$P_{2PA} \propto P_{Photon1} \cdot P_{Photon2} \propto I^2 \quad (2)$$

A comparison with the Jablonski diagram for 2PA in Figure 4 shows that the energy of a single photon is no longer sufficient to put an atom into an excited state. For this reason, the two-photon absorption can only take place in the region of the highest photon density. This lies exactly at the focal point of the laser light (Figure 3 on the right side). The region in which the 2PA takes place is described by the coefficient  $\sigma$  and has the dimension GM<sup>1</sup> (named after Maria Göppert-Mayer) [18–20].

---

<sup>1</sup>1 GM  $\equiv \frac{10^{-50} \text{ cm}^4 \text{ s}}{\text{photons} \cdot \text{molecule}}$

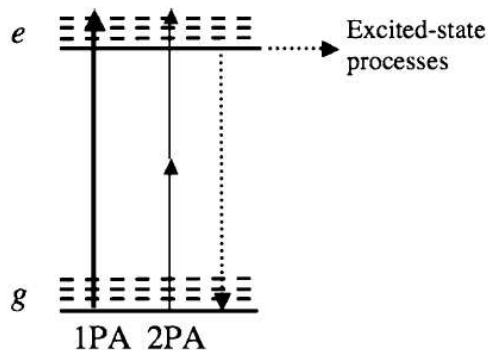
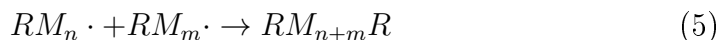
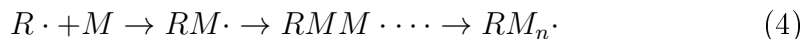


Figure 4: Simplified representation of the energy band model for 1PA and 2PA. Also known as a *Jablonski Diagram* [19]

To conclude this rather complex chapter, the most important points are summarized here. The DLW is based on two-photon absorption, as the absorption behavior is not linear. This means that, unlike with one-photon absorption, a photon alone is not absorbed by the photoresist and therefore polymerization only takes place at the focal point of the laser light. This makes it possible to create free-standing three-dimensional structures.

### 2.1.2 Two-Photon Polymerization

With the help of a femtosecond laser, the photochemical process of 2PP is activated in a small volume of the light sensitive resist. 2PP takes place when two photons are simultaneously absorbed by the photoinitiators  $PI$  (sensitizer in the photoresist) at the same time. The absorption energy puts the  $PI$  into an excited state  $PI^*$  and decomposes them into radicals  $R\cdot$ , which initiate the reaction. After their formation, the radicals combine with the monomers  $M$  to form monomer radicals  $RM$  and continue to propagate. When two pairs of monomer radicals combine, the polymerization process is terminated, as shown in the following equations [21].



To conclude this topic, Figure 5 compares the light intensity distribution of 1PA (red) and 2PA (blue). To start the polymerization process, a material-dependent limit must be exceeded.

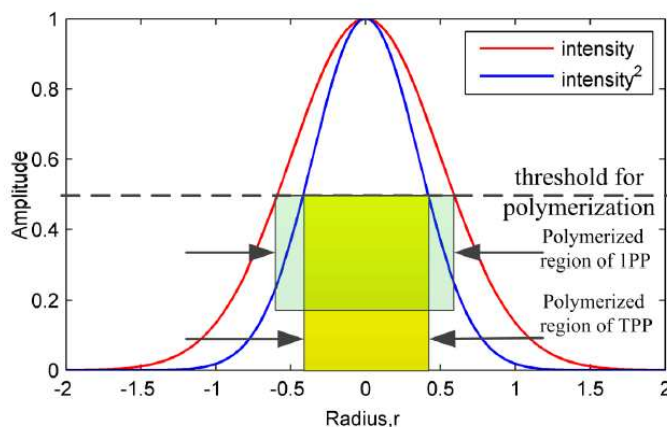


Figure 5: Distribution of intensity. [22]

## 2.2 Pyrolysis

Pyrolysis is the thermal decomposition of an organic material into its carbon skeleton in the absence of oxygen. The properties (such as chemical, mechanical, electrical) of the resulting carbon material depend on the previous material and the pyrolysis conditions. Important parameters are heating rate, maximum temperature and its holding time, vacuum level or gas flow rate [23].

During pyrolysis, all non-carbon atoms are removed from the polymer matrix. This results in a loss of mass and therefore also shrinkage. Furthermore, the process parameters are responsible for whether porous or dense C-structures are formed. As the temperature increases, pyrolysis can be divided into different stages: Degassing, radical activation, C-C bond formation and further graphitization [24].

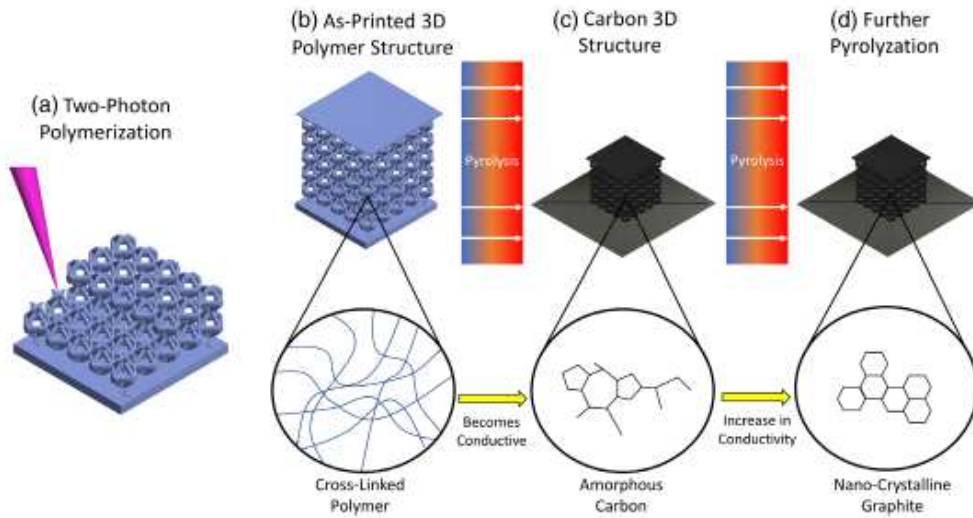


Figure 6: Process flow of pyrolysed carbon fabrication [25]

The production of ceramic or carbon structures via pyrolysis offers decisive advantages: The soft polymer material can be brought directly into a hard, robust and conductive form. Furthermore, extremely small dimensions can be achieved through the sometimes extraordinary shrinkage, which are difficult or impossible to realize by other methods [26].

As only the IP-Dip photoresist [17] was used in this work, the following description refers specifically to the pyrolysis of this photoresist.

When a polymer is heated above its degradation temperature, all volatile

components are released and a carbon skeleton, or more precisely glassy carbon, remains. This is shown schematically in Figure 7.

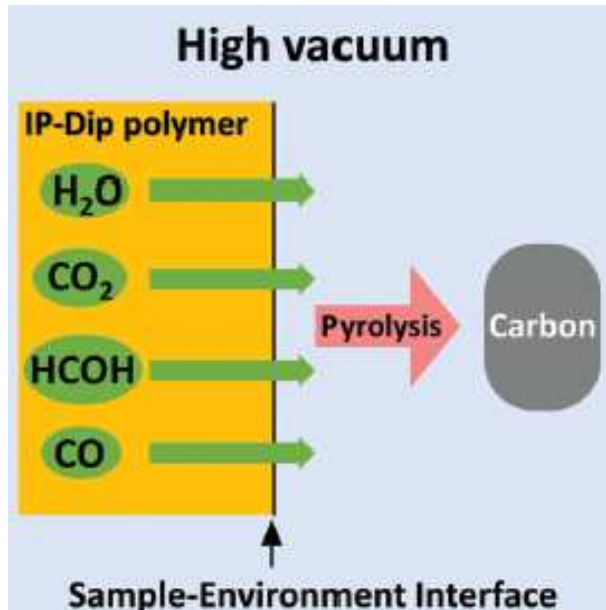


Figure 7: Pyrolysis of IP-Dip. Adapted from [24]

The molecular formula for IP-Dip is  $CH_2N_{0.001}O_{0.34}$  [27], which means that glassy carbon remains after pyrolysis. Extremely high shrinkage rates of up to 90% [26] are achieved.

### 2.3 PVD - Magnetron sputtering

One of the best-known and most widely used technologies for the production of thin films is physical vapor deposition (PVD). With the help of thin films, materials can be perfectly aligned for their application. Coatings can be used to improve tribological and optical properties as well as increase hardness.

As can be seen from Figure 8, PVD can be divided into two categories, evaporative PVD and sputtering PVD. Of the individual processes, magnetron sputtering is probably the most commonly used and therefore the following description refers specifically to it [28].

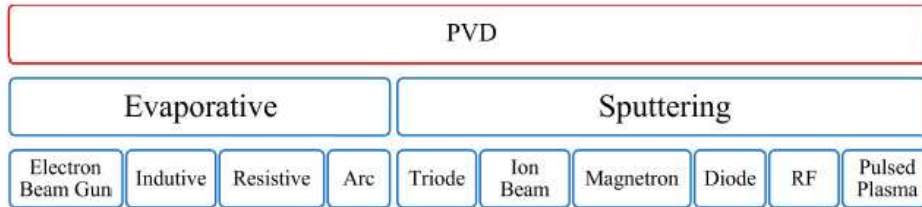


Figure 8: Overview of the major PVD techniques [29]

In general, all PVD sputtering processes work according to the same principle. The material to be coated, the substrate, is connected as the anode and the material to be deposited, the target, as the cathode. An inert gas (e.g. Ar) is continuously fed into the vacuum chamber, the molecules of which are converted into positively charged ions. The ejected electrons can ionize other gas atoms, creating a stable plasma. The ions hit the target material and release molecules, which are then accelerated to the substrate. The material condenses on the substrate and a coating is formed.

Figure 9 shows the basic setup of a magnetron sputtering coating system. In this process, permanent magnets (*magnetrons*) are arranged under the target in such a way that a magnetic field is formed near the target material. This magnetic field concentrates the electrons and causes them to move along the magnetic flux lines. This is known as balanced magnetron sputtering and has the advantage of increasing efficiency by increasing the number of impacts on the target [30].

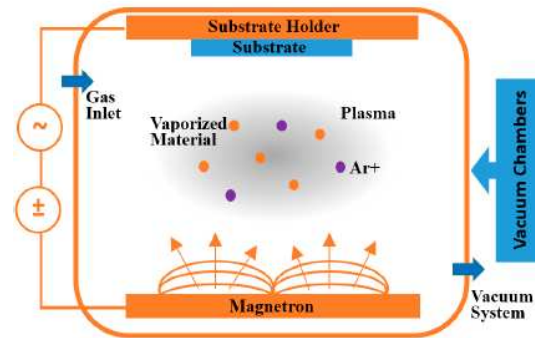


Figure 9: Schematic setup of a magnetron sputtering device [28]

To conclude this topic, André Anders structural zone diagram [31] is shown. In order to estimate the nature of the coating, he compares key parameters such as temperature and energy.

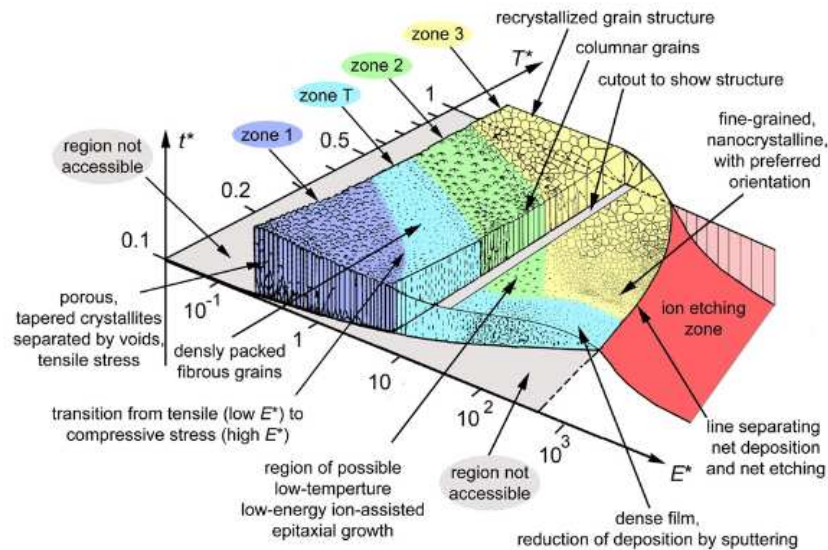


Figure 10: Anders structure zone diagram [31]



## 2.4 Focused Ion Beam milling

The FIB device is similar to a scanning electron microscope, with the difference that the beam that is scanned over the sample is an ion beam and not an electron beam. Most modern FIB devices supplement the FIB column with an additional SEM column, so that the device becomes a versatile *dual-beam* platform (FIB-SEM) [32].

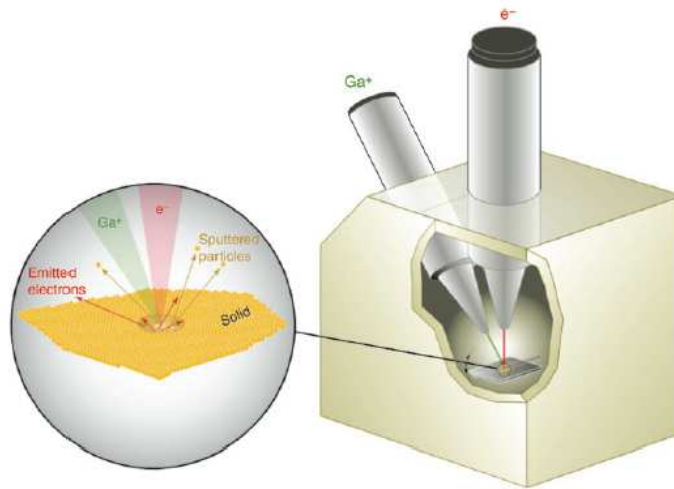


Figure 11: Setup of a dual-beam platform (FIB-SEM) [32]

The ion beam is focused to a diameter of 5-10 nm using electric and magnetic fields. Secondary electrons are generated by the interaction of the ion beam with the sample surface and can be used to obtain high-resolution images. Just like a cannonball removing bricks from a castle wall, an ion hitting a sample will knock out atoms. This is commonly referred to as sputtering and when performed in a controlled fashion, ion milling [33].

The ion source type used in all commercial systems and in the majority of research systems is the liquid metal ion source (LMIS). There are a number

of different types of LMIS sources, the most widely used is a Gallium-based source. Ga has decided advantages over other LMIS metals because of its combination of low melting temperature, low volatility and low vapor pressure. Figure 12 shows the comparison of the impact range of different species of ions [34].

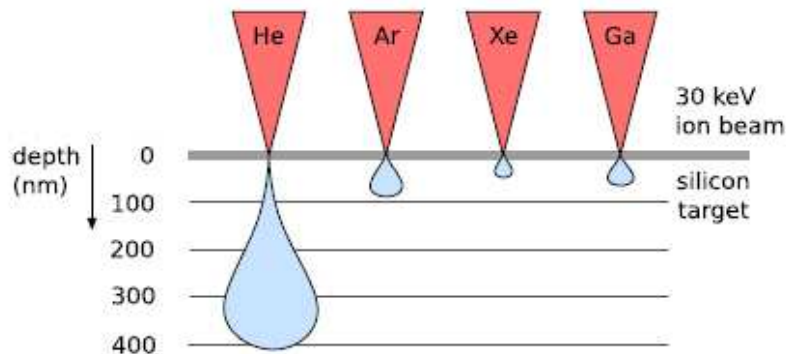


Figure 12: Comparison of different ion species [34,35]

## 2.5 In situ transmission electron microscopy

Max Knoll and Ernst Ruska [36] developed the first TEM in 1931, and since then scientists around the world have been trying to increase the resolution ever further. Nowadays, resolutions in the sub Ångstrom<sup>2</sup> range [37] are possible. Furthermore, the TEM was combined with external stimuli, which ultimately led to *in situ*<sup>3</sup> transmission electron microscopy.

In situ transmission electron microscopy allows direct observation of the sample's behaviour under external stimuli in real time [38]. Nowadays, there are

<sup>2</sup>1 Å = 0.1 nm

<sup>3</sup>in situ (lat.) - in the original position, in place

many different systems that allow the specimen's behaviour to be investigated. These include the evaluation of the dynamics during mechanical strain or deformation [39], the material behavior during heating or cooling [40], as well as the influence of the environment [41].

Figure 13 shows an overview of various factors that influence a sample, as well as other possible applications of in situ transmission electron microscopy.

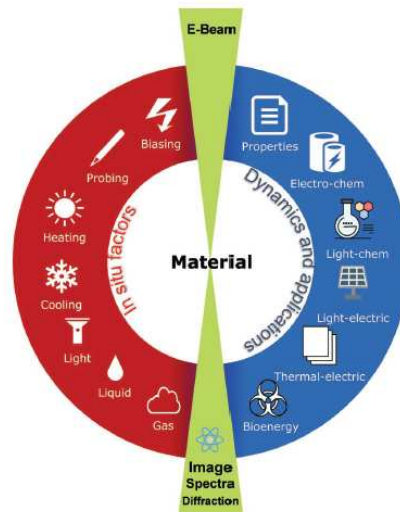


Figure 13: Overview of in situ factors and applications [42]

### 3 Experimental procedure

All models in this work were created using the Photonic Professional GT2 3D printer from NanoScribe GmbH. To create structures in the micro- and nanometer range the small feature solution set was used. The solution set consists of a lens with 63x magnification (the printer itself has a magnification of 10, so the total magnification is 630), a universal sample holder and the negative photoresist IP-Dip.

To develop and clean the samples after printing, PGMEA (propylene glycol monomethyl acetate, respectively 1-methoxy-2-propyl acetate) and isopropanol (2-propanol) were used.

There are basically two different methods to model structures. One is to use the printer's own software, DeScribe, in which you can create components with the highest possible resolution with just a few lines of code. The other option is to design the models in a CAD (*computer aided design*) program and then export them to the appropriate .stl (*standard transformation language*, respectively *standard triangulation language*) format. In this thesis, both methods were used, and the CAD program used was Inventor Professional 2021 from Autodesk [43].



Figure 14: Photonic Professional GT2 [17]



Figure 15: Small feature solution set as delivered [17]

### 3.1 Fabrication of nanoscale deformation structures

As described before, the models had to be sketched in CAD before the actual printing process. The 3D model can be seen in Figure 16. The push-to-pull device consists of a double rhombus and a platform. This model was transformed into the correct format (.stl) so that the printer can process it. All settings, such as print speed, laser power, and hatching & scaling could be made in the DeScribe software. The gridded tensile sample was also added in the DeScribe software to achieve the highest possible resolution.

After the printing process was completed, the sample was developed in PGMEA and isopropanol. Finally, a 100 nm thick copper layer was deposited by magnetron sputtering. The final specimen can be seen in Figure 18.

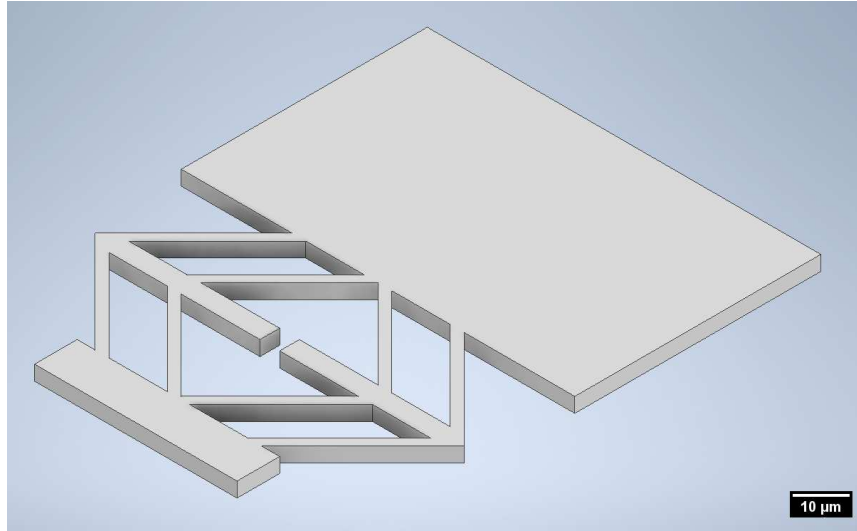


Figure 16: CAD model of the PTP device sketched in Autodesk Inventor Professional 2021, without the tensile sample.

### 3 EXPERIMENTAL PROCEDURE

---

As can be readily seen in Figures 17 and 18, structures programmed in the DeScribe software can be extremely small in size while maintaining high resolution.

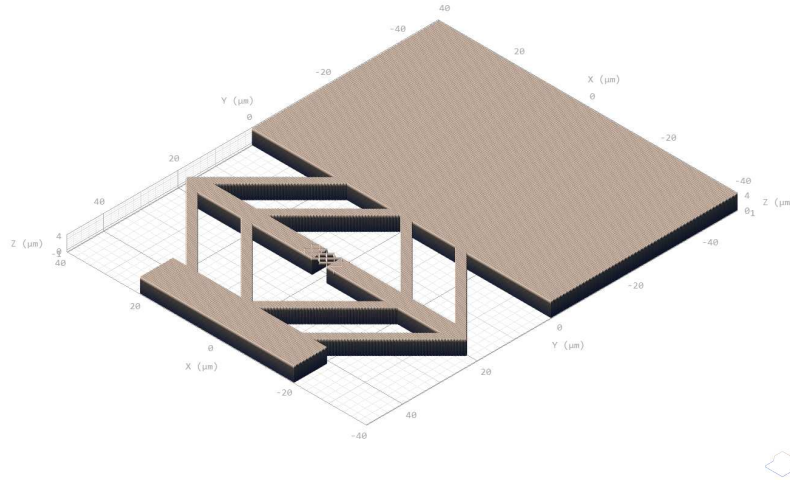


Figure 17: PTP device with the tensile sample added in DeScribe.

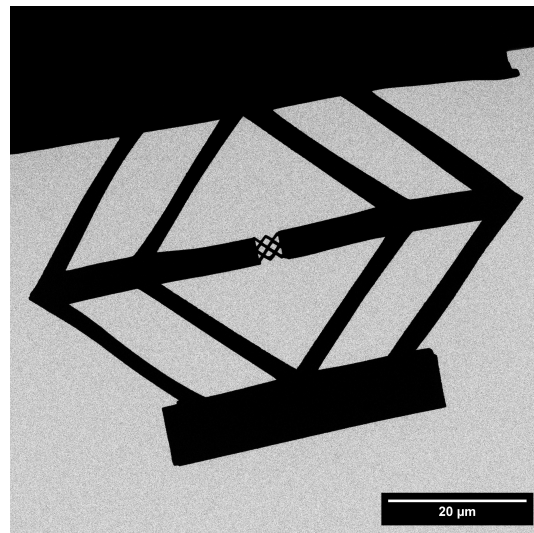


Figure 18: PTP device imaged in the TEM.

### 3.2 Comparison of different pyrolysis temperatures

In order to be able to investigate the effects of pyrolysis on the printed structures more closely, various test geometries were created, which can be seen in figure 19. The geometries include a cube, a cylinder, a cuboid, a rhombus, a hexagon, as well as hollow cubes and hollow cylinders. Since it is advantageous for the evaluation to proceed with average values or statistics, the same structures were printed several times.

To ensure unrestricted shrinkage as far as possible, the parts were placed on a relatively large block and this block in turn was placed on spiral springs. The springs, which were also created in DeScribe to achieve the most precise resolution possible, can be seen in Figure 20.

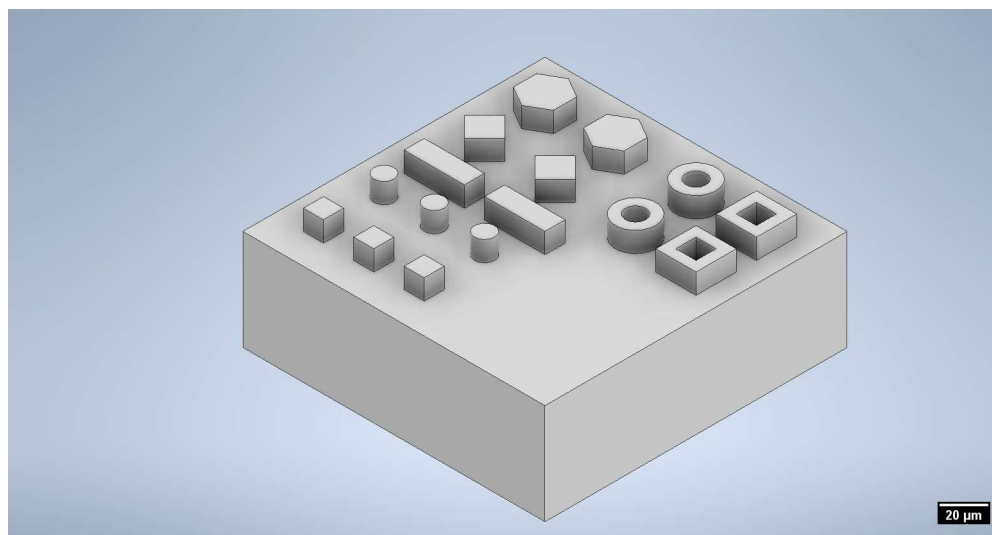


Figure 19: CAD model of the test geometries

### 3 EXPERIMENTAL PROCEDURE

---

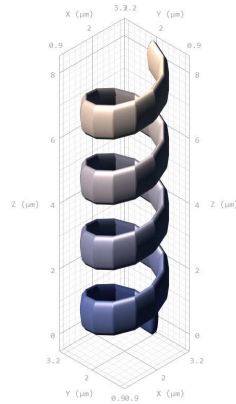


Figure 20: Spiral constructed in DeScribe to ensure unrestricted shrinkage.

Figure 21 shows the combination of the test geometria, block and springs in the DeScribe software. The block was placed on a total of 30 x 30 springs, spaced  $5\mu\text{m}$  apart. This was necessary to ensure sufficient adhesion between the printed structure and the substrate.

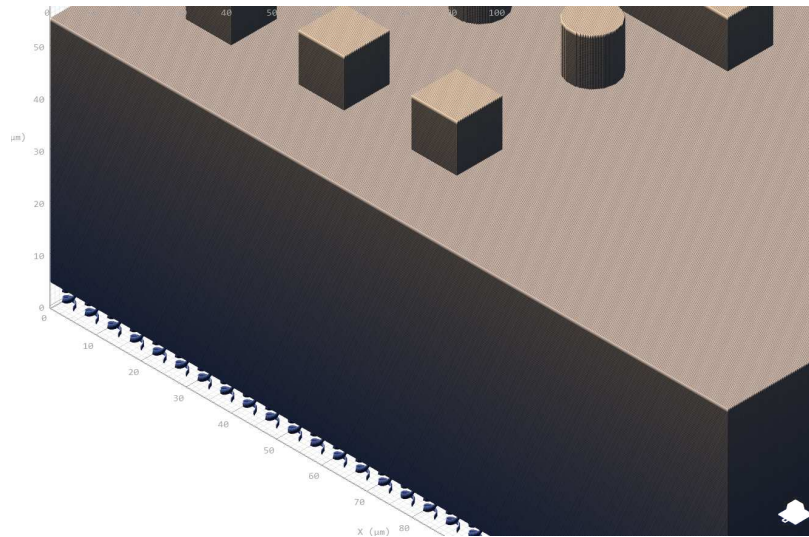


Figure 21: Combination of the test geometries and the spirals



The diagram below shows the schematic temperature profile of the pyrolysis. All samples were heated in the vacuum oven at 10 degrees per minute to their respective pyrolysis temperatures. After a two hour holding time, the heater of the furnace was turned off and the sample was cooled in vacuum to room temperature. The pressure in the vacuum oven was approximately  $5 \times 10^{-6}$  millibar throughout the cycle.

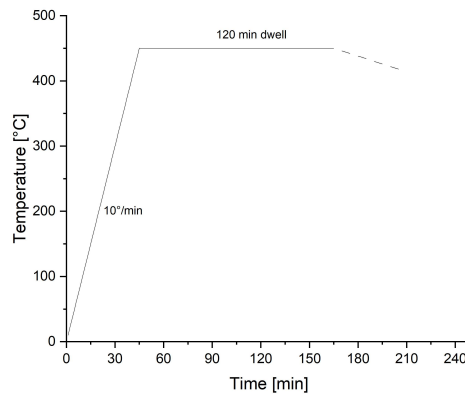
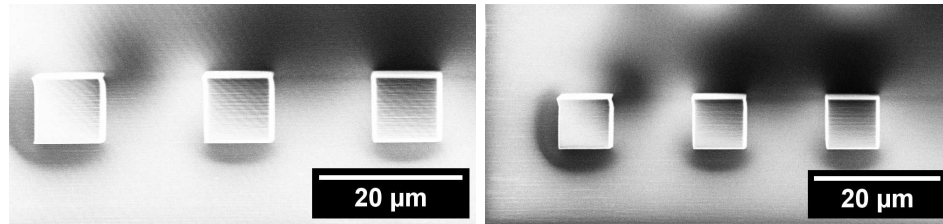


Figure 22: Temperature profile used for pyrolysis

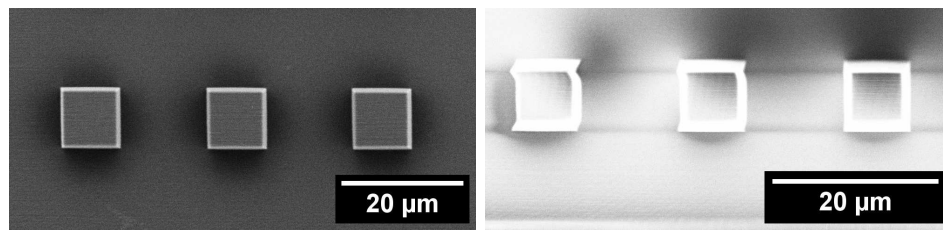
The following SEM images (Figure 23a - 23f ) show the cube-shaped test structures after different pyrolysis temperatures, as well as a reference sample which was not pyrolysed. Considering the changing scale, it is easy to see that shrinkage has occurred. Furthermore, the dimensional stability, with free shrinkage, is also fulfilled over a wide temperature range.

In Figure 23a it can be seen that the initial side length of the cube was 10  $\mu\text{m}$ . As can be seen from Figure 23b and 23c, no significant size change occurs at lower pyrolysis temperatures up to 350°C. Only higher temperatures lead to a significant dimensional change. This behaviour could be observed for all test geometries. After a temperature of about 500°C, the pyrolysis process is complete.



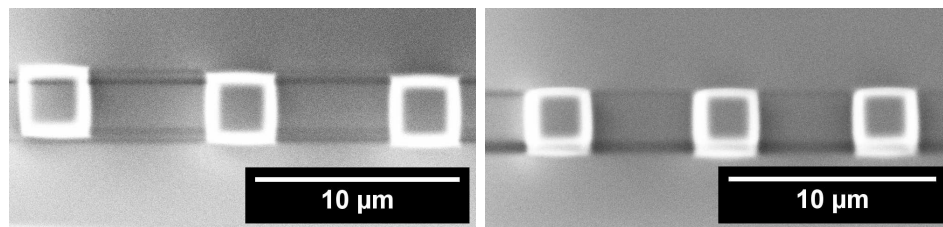
(a) Reference sample

(b) Pyrolysis at 300°C



(c) Pyrolysis at 350°C

(d) Pyrolysis at 400°C

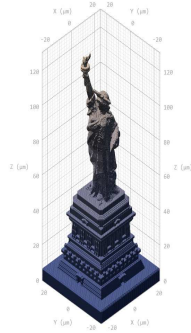


(e) Pyrolysis at 450°C

(f) Pyrolysis at 500°C

Figure 23: SEM images show shrinkage after different pyrolysis temperatures. Please note the different scale bars at 450°C and 500°C

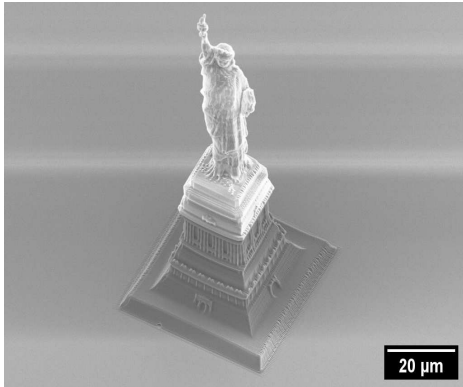
To further illustrate the process of pyrolysis, a model [44] of the famous Statue of Liberty of America was printed and then pyrolysed. In Figure 24, the effect of different temperatures can be clearly seen. The extremely high resolution of the printer can be seen, as well as the enormous shrinkage at high pyrolysis temperatures.



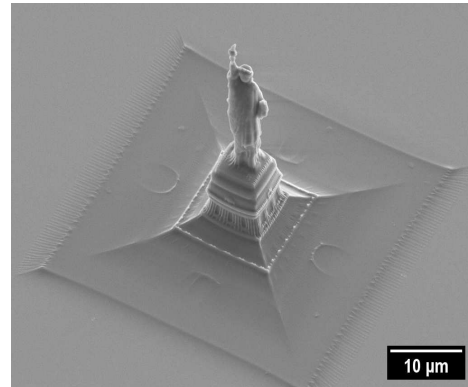
(a) DeScribe model (adapted from [44])



(b) Pyrolysed at 350°C



(c) Pyrolysed at 400°C



(d) Pyrolysed at 500°C

Figure 24: Statue of Liberty at different pyrolysis temperatures. Please note the different scale bar at 500°C

### 3.3 Design optimization for isotropic shrinkage

In this chapter, we will discuss the procedure for designing a support that allows isotropic shrinkage. From the previous chapters it is clear that for optimal pyrolysis of the samples, the correct temperature and holding time must be selected, but it must also be ensured that the components can contract as far as possible without restrictions. Theoretically, there are many ways to meet these requirements. However, the goal here was to obtain a robust and reproducible result with as little effort as possible.

At the beginning, a test run was carried out using pillars representing geometrically simple supports. Figure 25 shows the model of the specimen. Figure 27 and 29 show SEM images of the sample after pyrolysis. The support columns have fulfilled their purpose and an unrestricted reduction in size has occurred. It should also be noted that the material can withstand immense strain. Figure 29 shows the specimen imaged from the side at a 30° angle. It is noticeable that the specimen shows bending and is therefore also in contact with the substrate.

In a second test the pillars were replaced by spirals. Figures 26, 28 and 30 show the model and the SEM images of the sample after pyrolysis. The test structure was placed on the same coil springs (see Figure 20) used in Section 3.2. A total of 24 springs, which were evenly distributed, were used. Figure 28 shows that even more extreme shrinkage was realized here. However, it can be seen in Figure 30 that the specimen again exhibits bending and is thus in contact with the substrate. Likewise, on closer inspection, it can be seen that some springs have been torn off due to the enormous reduction in size of the specimen.

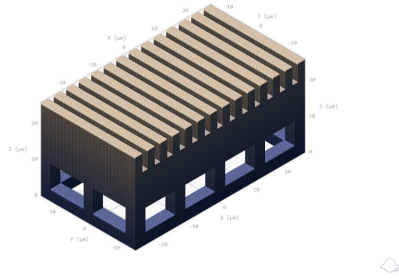


Figure 25: Test structure on pillars

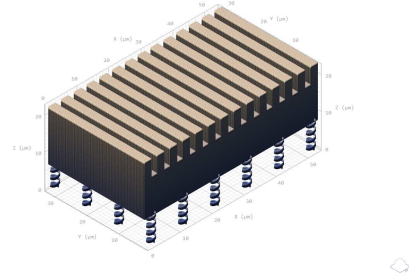


Figure 26: Test structure on spirals

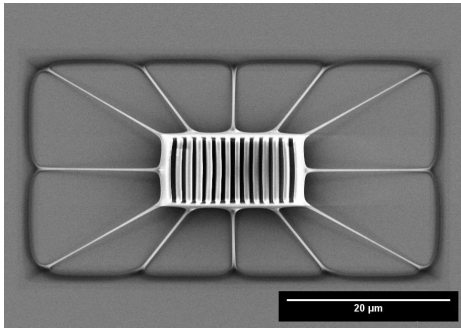


Figure 27: Test structure on pillars after pyrolysis

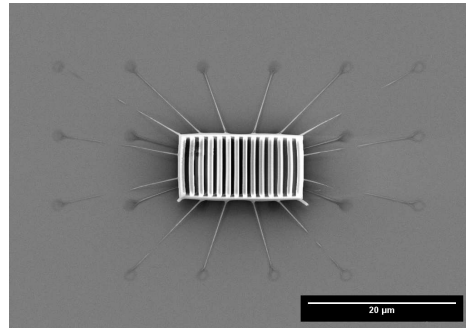


Figure 28: Test structure on spirals after pyrolysis

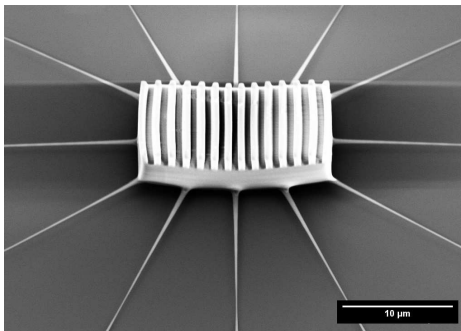


Figure 29: Test structure on pillars imaged at 30° angle

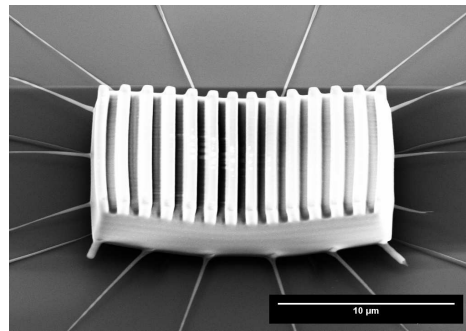


Figure 30: Test structure on spirals imaged at 30° angle

In the third test run, an entirely different concept was used. The substructure was chosen much larger than in the previous tests and has the shape of a great rhombic cuboctahedron. The model was adapted from thingiverse [44]. The symmetry of the base is intended to ensure isotropic shrinkage and further, due to the large distance between the test structure and the substrate, to prevent the contact of these two after pyrolysis. Figure 31 shows the DeScribe model of the test structure and Figure 32 the resulting SEM image of the sample after pyrolysis.

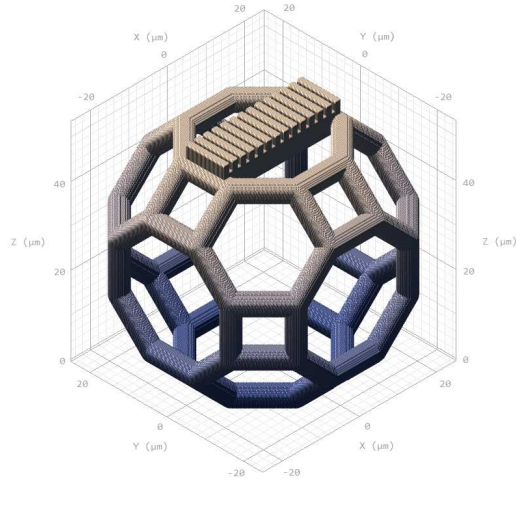


Figure 31: DeScribe model of a test structure on a rhombic cuboctahedron

Here, all requirements for the successful test were met. Thanks to the symmetry of the substructure, isotropic shrinkage took place. Furthermore, the test structure could contract largely without restriction, since the base itself can fold inwards and shrink enormously while maintaining symmetry. In conclusion, the enlarged substructure allows isotropic shrinkage, offers a robust support and prevents the test structure from contacting the substrate after pyrolysis.

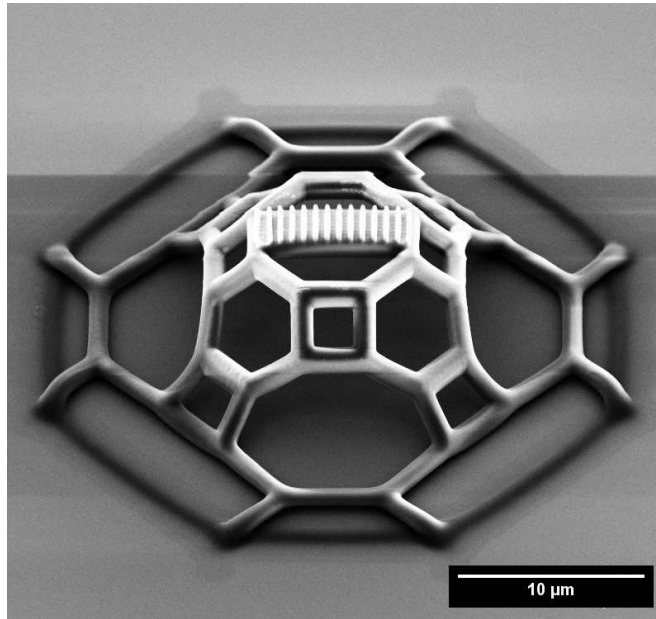


Figure 32: Test structure on a rhombic cuboctahedron after pyrolysis at 450°C

Now that a working prototype was developed, the final sample could be designed, printed, and pyrolysed for further testing. This will be discussed in the following.

### 3.3.1 Final sample design

As can be seen in Figure 33, the test structure has been enlarged and now has a square base. This is to guarantee that there is enough space afterwards to be able to cut out a sample with the FIB. The base was again a large rhombic cuboctahedron. The base was enlarged by a factor of 1.5 to offer even greater stability during pyrolysis.

### 3 EXPERIMENTAL PROCEDURE

---

Figure 34 shows a SEM image of the final sample after pyrolysis. A temperature of 450°C and a holding time of 2 hours were selected to ensure that the pyrolysis process was completed. As can be clearly seen, the sample has fulfilled all the requirements. It has isotropically shrunk, does not show bending, is not in contact with the substrate and has enough space to cut out a deformation specimen with the FIB. Finally, the free-standing lines and gaps, which are going to be filled with copper in the next step, can be clearly seen.

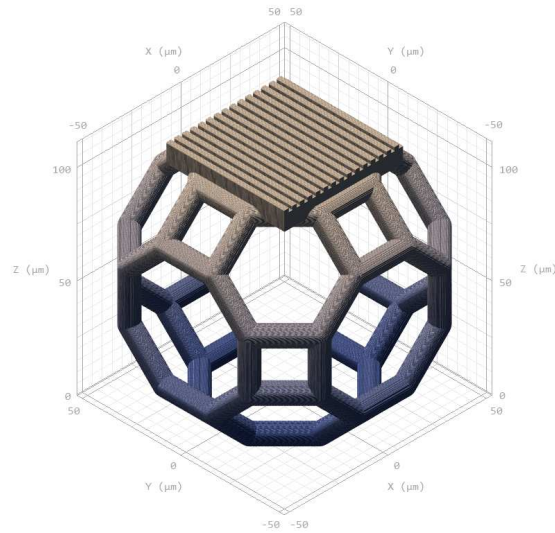


Figure 33: DeScribe model of the final structure



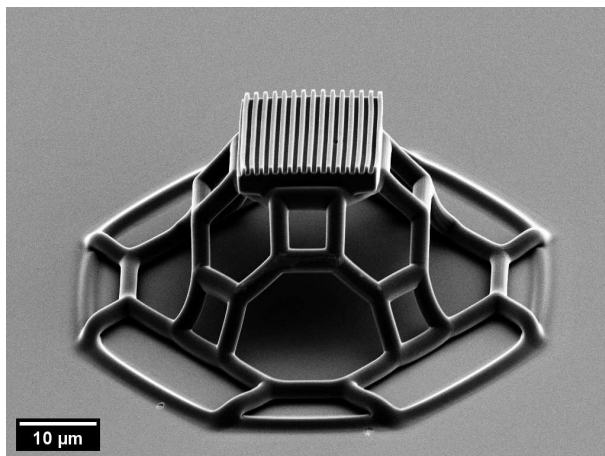


Figure 34: Final structure after pyrolysis at 450°C

### 3.4 Coating procedure

All coatings in this work were done with a thin film deposition system from Korvus Technology [45], see Figure 35. With this deposition system, the required layers can be deposited in a short time and up to two different targets can be used at the same time (Figure 36). For the coatings in this work, only a single copper target was used. This type of deposition is PVD (*physical vapor deposition*), more precisely magnetron sputtering. Table 1 below summarizes the parameters used for the coatings of the samples.



Figure 35: Thin Film Deposition System [45]

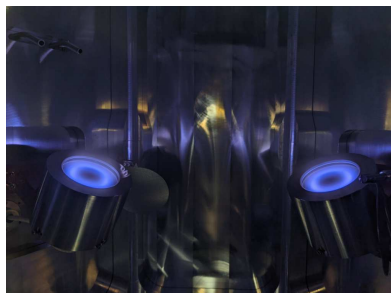
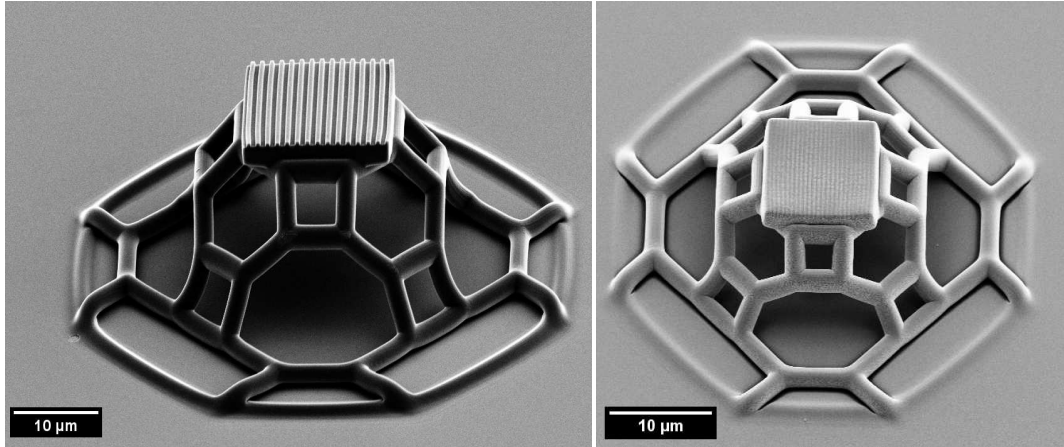


Figure 36: Targets during deposition process [45]

Table 1: Parameters for magnetron sputtering

Parameter	Value	Unit
Power	40	W
Ar gas flow	20	sccm
Rotation speed	20	rpm
Temperature	Room temperature	°C
Duration	100	min
Pressure before deposition	$2.5 \times 10^{-5}$	mbar
Pressure during deposition	$1.6 \times 10^{-3}$	mbar

### 3.4.1 Filling grade depending on the sample geometry



(a) Before sputtering

(b) After sputtering

Figure 37: SEM images for comparison before and after coating

Figure 37 shows the sample before and after the coating with 1  $\mu\text{m}$  of copper. It can be seen that the coating follows the structure of the sample. It is, however, difficult to asset whether the gaps between the lines are filled.

Therefore, for each sample geometry a FIB cross-section was cut. A protective Pt layer was deposited in the FIB to prevent curtaining during FIB cutting. As can be clearly seen, the geometry has a very strong influence on the filling condition. Figure 38 shows a SEM image of a completely and partially filled structure.

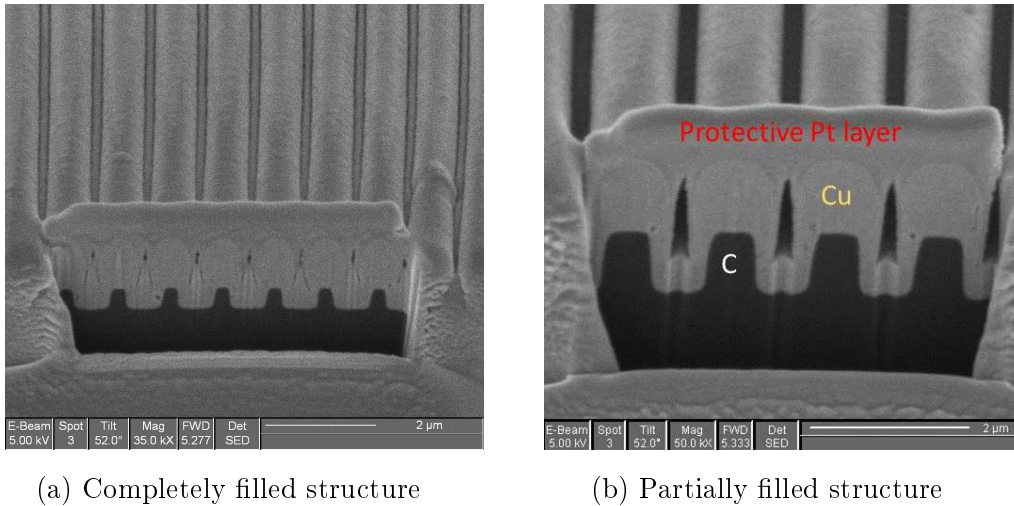


Figure 38: SEM images of completely and partially filled structures

The strong dependence on geometry can be explained by the fact that those copper atoms which condense on the sample as a thin film impinge on the sample at an angle of approximately  $30^\circ$ . The angle is determined by the design of the coating system. If there is a large height to width ratio, the gap cannot be completely filled.

The developed working manufacturing process allows to produce tailored metal-carbon composites. To test the mechanical properties, in-situ testing in the TEM was performed as described in chapter 4.5. To summarize the experimental procedure, Figure 39 shows the workflow from printing to testing the samples.

## 3.5 Workflow

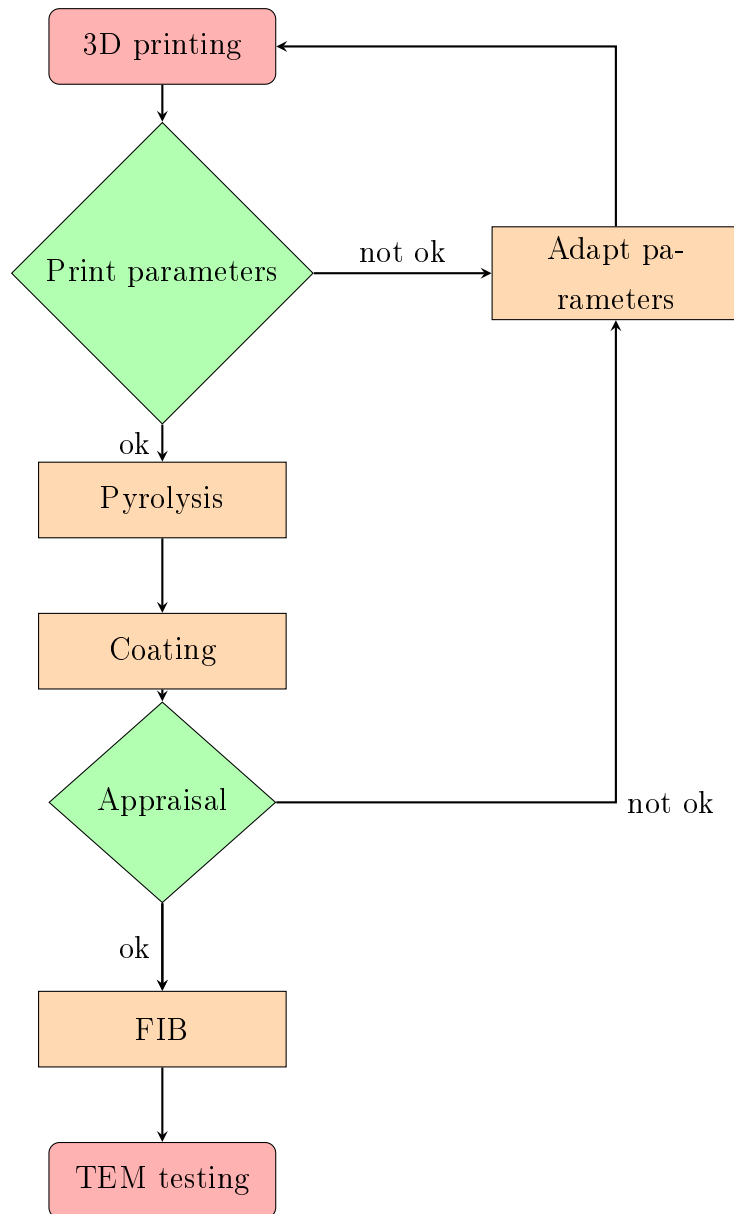


Figure 39: Workflow chart from 3D printing to testing

## 4 Results and discussion

This chapter consists of a total of four parts in which the results of this work are discussed. The first part shows the deformation of nanoscale deformation structures. In the second part the results of the different pyrolysis temperatures and their influence on the shrinkage behavior are described. In the third part the degree of filling and its dependence on the sample geometry is briefly shown and in the last part the fabrication of a metal-carbon nanocomposite bending specimen is discussed.

### 4.1 Results of the nanoscale deformation structures

Figure 40 shows the nanoscale deformation structure before and after the failure of the sample. At the bottom of the image you can also see the tip of the nanoindenter with which the experiment was performed.

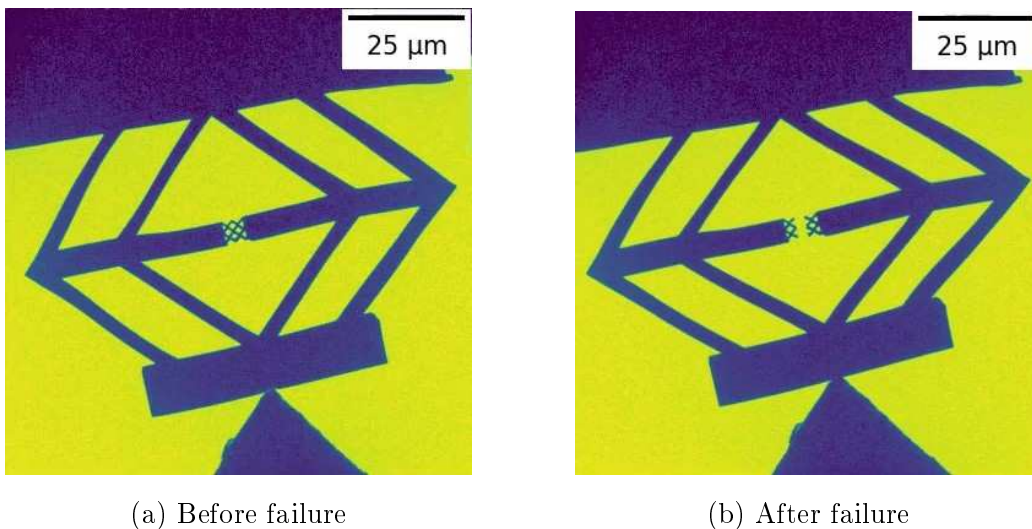


Figure 40: Nanoscale deformation structure before and after the failure of the sample

The raw data recorded during the test is shown in Figure 41. The load is plotted in  $\mu\text{N}$  over the displacement in nm. At the beginning of the test, the force increases almost linearly with deformation. After the specimen breaks, the load drops immediately and returns almost to zero. The structure was then subjected to further loading, allowing a second curve to be recorded to determine the stiffness of the deformation structure.

Therefore, two different curves were obtained, with curve 1 describing the behaviour of the specimen up to failure. Finally, the slope of curve 2 was used to determine the stiffness of the deformation structure without the specimen.

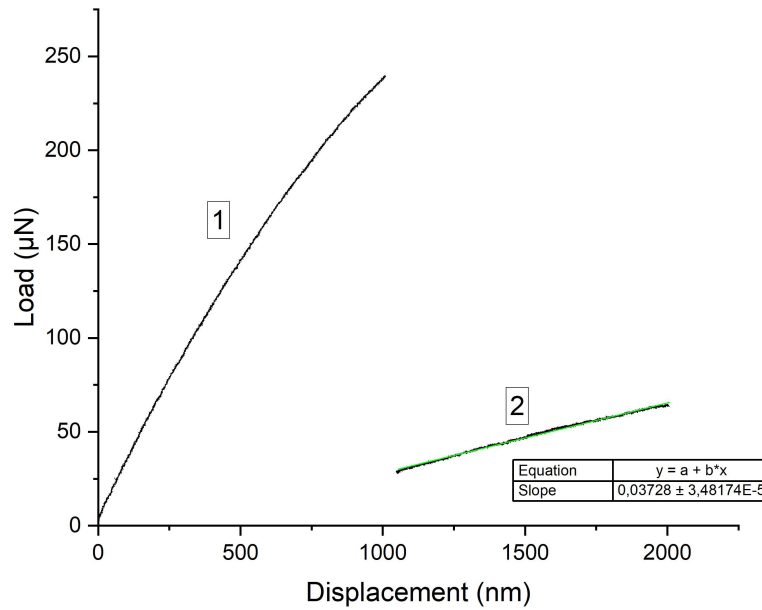
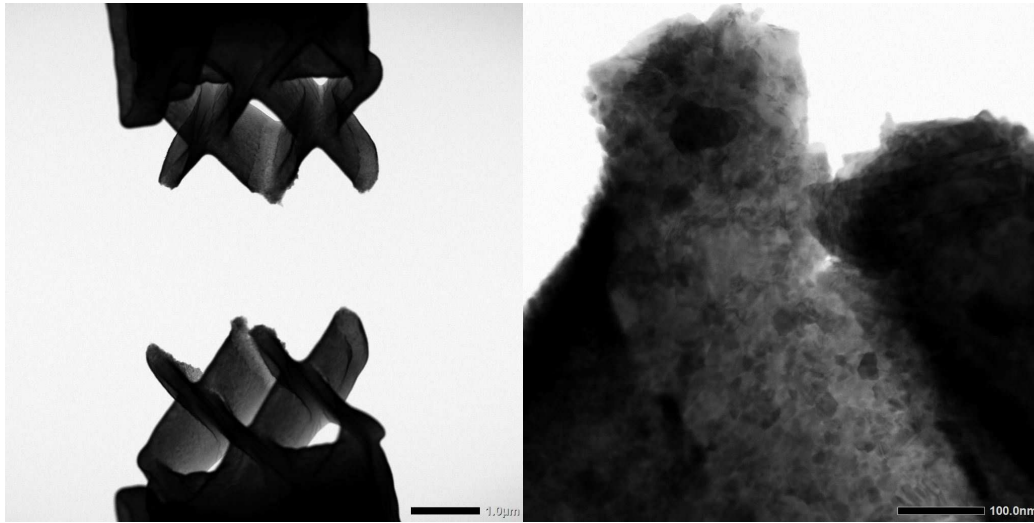


Figure 41: Raw load-displacement curve of the nanoscale deformation structures

The stiffness of the deformation structure was calculated at approximately  $37 \text{ Nm}^{-1}$ . The Bruker Nano Surfaces Division produces push-to-pull devices with similar deformation behavior in the stiffness classes 15, 150 and 450  $\text{Nm}^{-1}$  [46]. It can therefore be said that the printed PTP device offers useful deformation properties.

This ability to directly design and manufacture push-to-pull devices yourself offers many possible applications. Not only can the sample and the sample carrier be modeled precisely for the required functions, but several geometries can also be printed side by side. This makes it possible to test many structures in a short time, opening the possibility for high throughput testing.



(a) 20000x magnification

(b) 250000x magnification

Figure 42: Bright field scanning transmission electron microscope images of the fractured sample at two different magnifications

Figure 42 shows the tested specimen after failure at various magnifications. On the left-hand side you can see that the sample has broken as expected at the bars in the middle and not at the edges, which indicates that the printed sample is well attached to the PTP. The right side shows a higher magnification and the individual copper grains are clearly visible. There are also some twins, which either formed during the coating process or were formed due to the severe deformation during the test.

## 4.2 Evaluation of the pyrolysis experiments

The following diagram (Figure 43) was created to evaluate the pyrolysis experiments. The normalized area is plotted against the pyrolysis temperature. A normalized area of size 1 reflects a non-pyrolysed sample. The sample starts to shrink at 350°C and the process is completed at 450°C. This means that all volatile components have escaped from the sample. As mentioned in chapter 2.2, glassy carbon remains after the pyrolysis of IP-Dip. A longer heat treatment at higher temperatures causes the sample to pyrolyse further and nano-crystalline graphite will be produced.

Furthermore, an extreme reduction in the size of the samples was achieved through pyrolysis. After the experiment, the structures were only about 10% of their original size. This value agrees with the literature [26].

In order to obtain exact values, a so called Boltzmann fit, which is described by formula 6, was applied to the graph.

$$f(x) = \frac{A_1 - A_2}{1 + e^{(x-x_0)/dx}} + A_2 \quad (6)$$



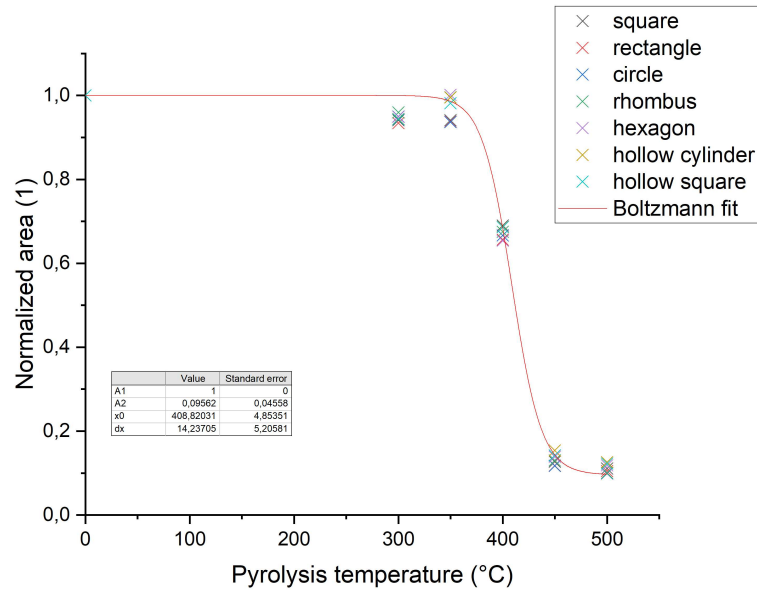


Figure 43: Boltzmann fit of the pyrolysed samples

Table 2 lists the variables of the Boltzmann fit and explains their meaning. As can be seen, the value for A2 is 0.095, which means that the area after pyrolysis is only about 10% of the original area.

Table 2: Results of the Boltzmann fit

Variable	Definition	Value	Unit
A1	Normalized Area without pyrolysis	1	1
A2	Normalized Area after pyrolysis	0.095	1
x0	Temperature where pyrolysis is 50 % finished	408	°C
dx	Shrinkage rate depending on temperature	14.24	1/°C

### 4.3 Filling grade in dependence of the sample geometry

A contour map, which is shown in Figure 44, was created to evaluate the filling level as a function of the sample geometry. For this purpose, a cross-section was produced for each geometry using FIB and the individual filling heights were measured. These measurement points are marked on the map and the rest of the chart was extrapolated using this data. In this way, the degree to which the gaps between the carbon lines are filled can be estimated in advance.

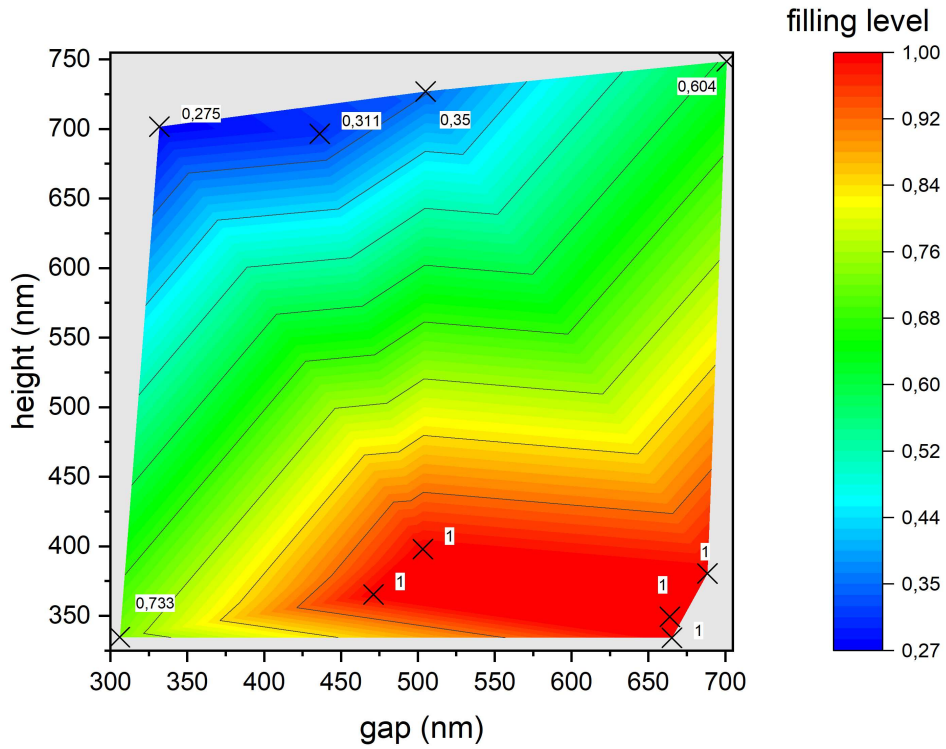


Figure 44: Filling grade depending on the gap to height aspect ratio

If there is a wide and shallow gap, it can be completely filled. Conversely, narrow, deep gaps are more difficult to fill. This behavior can be explained by the impact angle of the copper atoms, as described in more detail in chapter 3.4.1.

The great advantage of this contour map is the ability to estimate how the coating will behave on the sample surface before a sample has to be printed, pyrolysed and coated.

#### **4.4 Detailed TEM investigation of the tailored metal-carbon nanocomposites**

This chapter discusses step by step how to create a TEM specimen from the finished printed, pyrolysed and coated structure. A total of six steps (see Figure 45 - 50) are required to produce a TEM sample from the printed structure. In Figure 45 you can see the sample, which was pyrolysed at 450°C for 2 hours and coated with 1µm copper.

All steps concerning the Focused Ion Beam were carried out by Dr. Alice Lassnig with the Zeiss Auriga system, consisting of a focused ion beam column (Orsay Physics Ga<sup>+</sup> ion FIB) and a scanning electron column (Gemini Schottky field emission) at the Erich Schmid Institute of Materials Science.

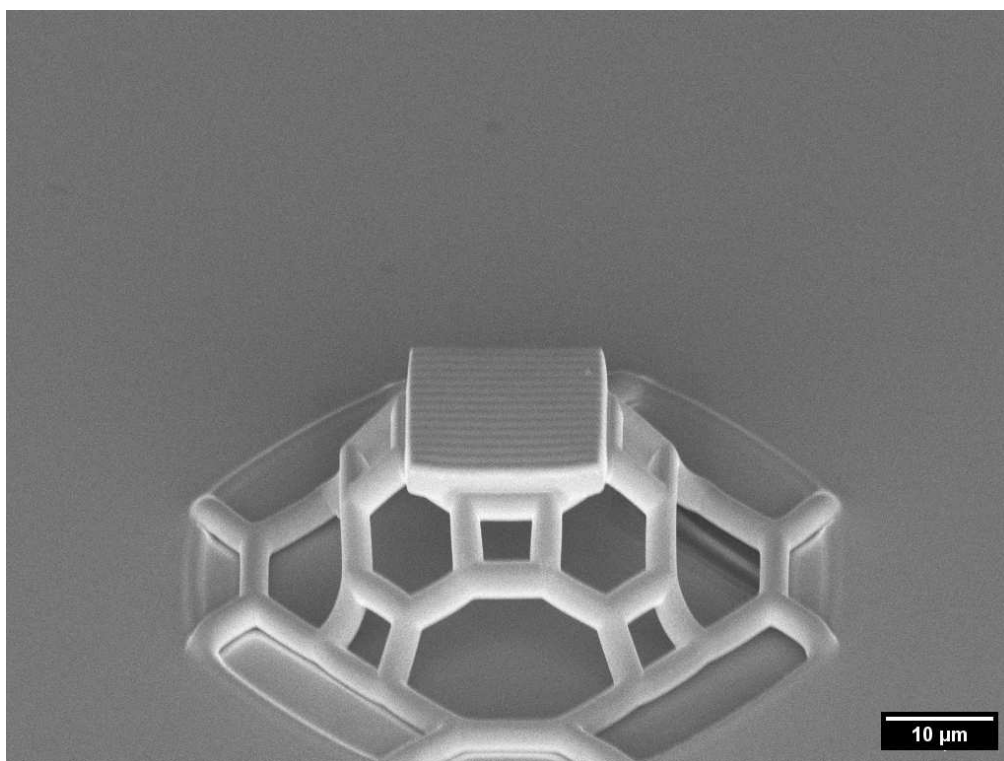


Figure 45: Final specimen coated with 1  $\mu\text{m}$  of copper

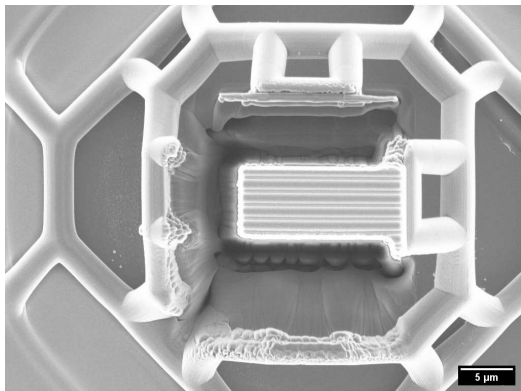


Figure 46: This Figure shows the structure from top view. As you can clearly see, in the first step the platform was cut from above on 3 sides and thus separated from the substructure. Now the carbon copper lamellas are only connected to the base structure on one side.

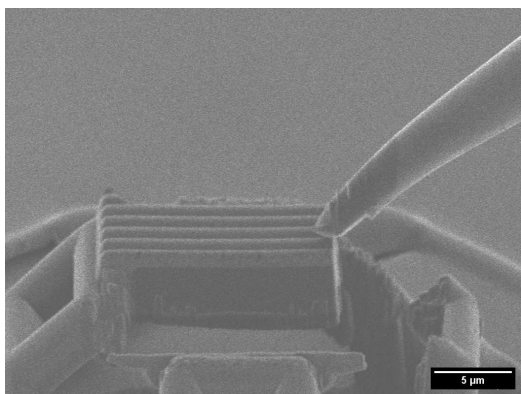


Figure 47: The nanomanipulator is now connected to the structure by platinum deposition and the remaining side is then cut through. In this way, the carbon copper composite can be transferred to a suitable sample holder.

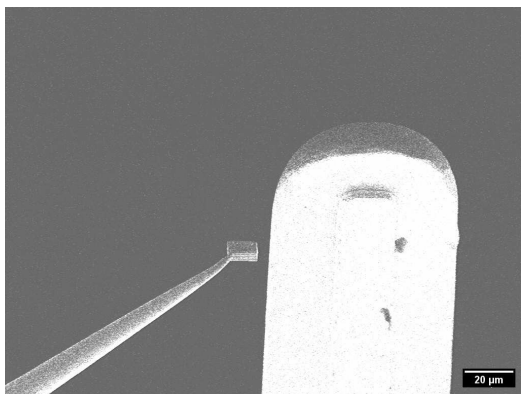


Figure 48: Once the nanomanipulator has been successfully attached, the sample can now be transferred to a sample holder suitable for the TEM. In this case, the sample holder was an Omniprobe lift-out grid.

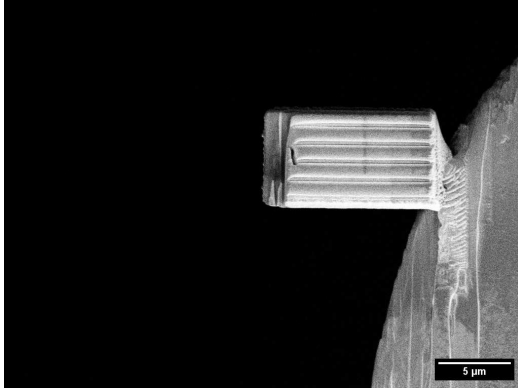


Figure 49: The sample is fixed to the sample holder and can now be processed further. The first step is to release the manipulator from the structure. As can be seen at the left end of the sample, a part of the sample is lost when the nanomanipulator is released.

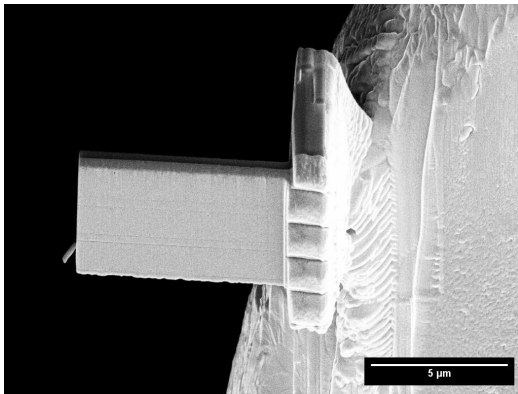


Figure 50: In this step, the sample is thinned to the desired thickness. A remaining part of the manipulator can also be seen, which is subsequently removed. The sample is thinned until the alternating carbon copper layers are visible.

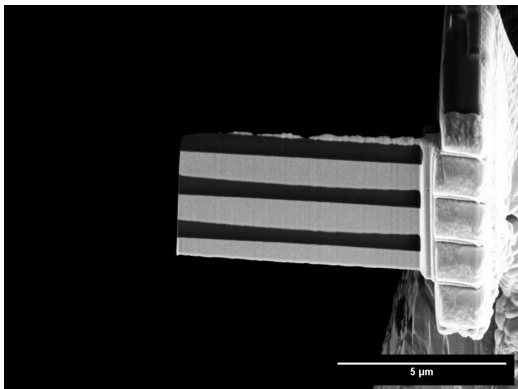


Figure 51: The finished sample can be mounted in the TEM.

Figure 52a shows a BF-STEM<sup>4</sup> image of the final sample in the TEM. There are three layers of carbon and three layers of copper. On the left side, the incision where the sample is to break can also be clearly seen. The experiments in the transmission electron microscope were carried out in the TEM JEOL 2200FS at the Erich Schmid Institute of Materials Science.

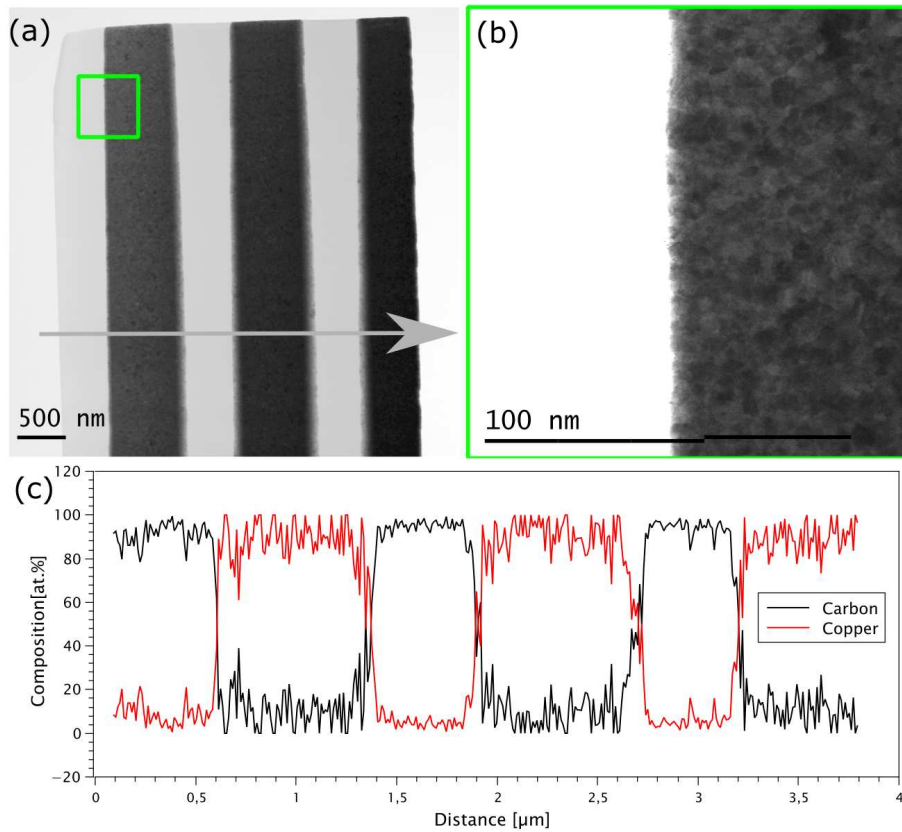


Figure 52: Final sample imaged in the TEM. (a) BF-STEM image. The area marked with a green square is magnified in (b). (c) EDS profile of the copper-carbon nanocomposite, the location is indicated with a grey arrow in (a).

<sup>4</sup>Bright field scanning transmission electron microscope

#### 4.5 In situ deformation of the tailored metal-carbon nanocomposites in the TEM

To study the deformation behavior of the Cu-C nanocomposite, in situ deformation was carried out in the TEM using a Bruker Hysitron PI95 nanoindenter holder. The composites were mounted on a Bruker PTP device allowing for controlled tensile deformation. A notch was made in the FIB to initiate crack propagation. Figure 53 shows a bright-field TEM image of the sample prior to loading. The loading direction is indicated with arrows. Figure 54 shows individual frames extracted from the in situ deformation test. Surprisingly, the crack propagates only slowly in the carbon layer after failure of the ductile Cu layer. This demonstrates that the combination of layers with different mechanical properties can lead to dramatically improved fracture resistance.

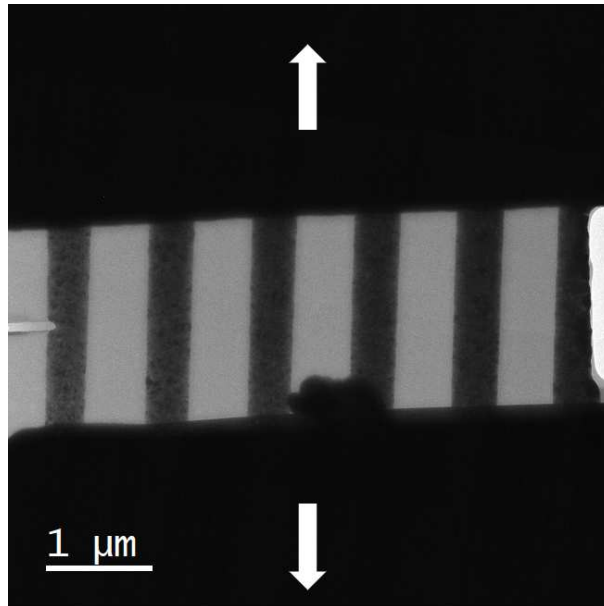


Figure 53: Bright field TEM image showing the Cu-C nanocomposite mounted for in situ tension in the TEM.



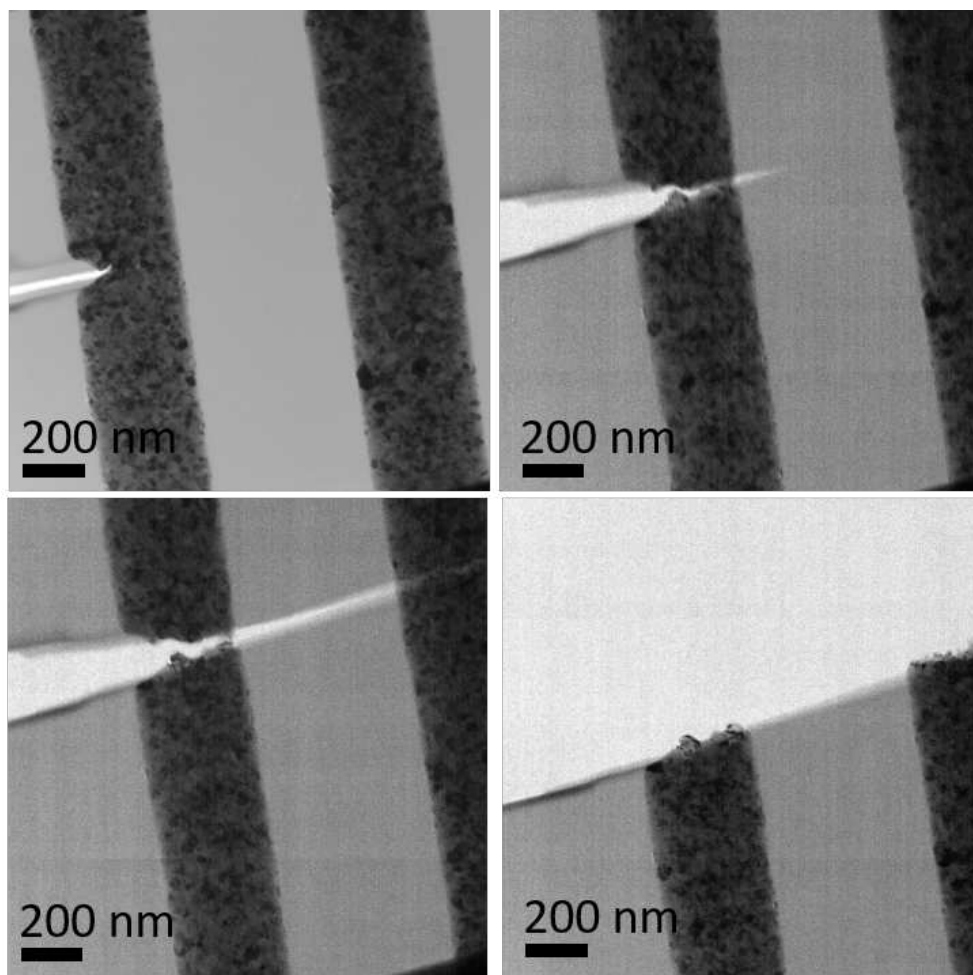


Figure 54: Bright-field TEM images acquired during in situ deformation in the TEM revealing slow crack propagation.

## 5 Conclusion and outlook

This work dealt with the direct production of deformation structures by means of two-photon polymerization on the submicrometer scale. In addition, carbon copper composites were fabricated using pyrolysis and magnetron sputtering.

The nanoscale push-to-pull devices exhibited very good, linear deformation behavior and a stiffness of approximately  $37 \text{ Nm}^{-1}$ . This allows to decouple the effect of the push-to-pull device from the structure to be tested. Finally, it is demonstrated that this new experimental design enables the possibility of high throughput testing in the TEM.

To produce the composite materials, the samples printed using DLW were first pyrolysed for two hours at  $450^\circ\text{C}$  and then coated with  $1\mu\text{m}$  copper using magnetron sputtering. The sample geometry proved to be an important parameter, as it determines whether the gap can be completely filled, which is a requirement for successful fabrication. It should also be mentioned that extremely small dimensions can be reached by pyrolysis, which cannot be achieved by DLW alone. TEM investigations revealed sharp well-defined interfaces between the Cu and C layers.

The final tensile test of the composite sample clearly shows that the composite shows attractive mechanical properties.

The importance of researching and understanding the phenomena at these length scales should be illustrated by the following examples. Tensile tests of aluminum-polymer composites showed that aluminum oxide, from a layer thickness below  $50 \text{ nm}$ , reach the range of the theoretical strength of  $5.5$

GPa [47]. Cellular metamaterial structures are excellent energy absorbers on the submicrometer scale. To optimize the design of these structures, one must be able to test the dynamic properties, such as storage and loss modulus, on this scale [48].

Finally, some ideas and possible experiments should be mentioned, which can be linked to the results of this work. For example, it would be interesting to print and test other forms of nanoscale deformation structures. Furthermore, nanocomposite materials could be produced with a different combination of materials in order to investigate the mechanical properties of e.g. metallic glasses or high entropy alloys.

## 6 Appendix

### IP-Dip

Table 3: Properties<sup>5</sup> of IP-Dip [17]

Property	Value	Unit
Young's modulus	2.91	GPa
Vickers Hardness	12.05	HV0.0025
Tensile strength	7.6	MPa
Shrinkage after polymerization	5-17	%
Density (liquid)	1.170 @ 20°C	$g/cm^3$
Density (solid)	1.26 @ 20°C	$g/cm^3$
Viscosity	2420 @ 20°C	mPas

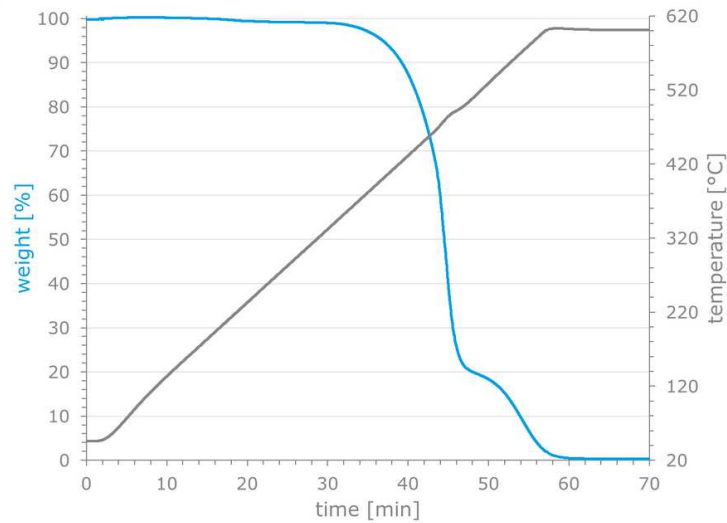


Figure 55: TGA analysis of polymerised IP-Dip [17]

<sup>5</sup>Parameters may vary depending upon several process parameters.

## References

- [1] James H. Strickler and Watt W. Webb. Two-photon excitation in laser scanning fluorescence microscopy. In Ronald L. Antos and Allen J. Krisiloff, editors, *CAN-AM Eastern '90*, SPIE Proceedings, pages 107–118. SPIE, 1991.
- [2] S. Maruo, O. Nakamura, and S. Kawata. Three-dimensional microfabrication with two-photon-absorbed photopolymerization. *Optics letters*, 22(2):132–134, 1997.
- [3] Julia Liu, Debashish Das, Fan Yang, Andrea G. Schwartz, Guy M. Genin, Stavros Thomopoulos, and Ioannis Chasiotis. Energy dissipation in mammalian collagen fibrils: Cyclic strain-induced damping, toughening, and strengthening. *Acta biomaterialia*, 80:217–227, 2018.
- [4] Franziska Klein, Thomas Striebel, Joachim Fischer, Zhongxiang Jiang, Clemens M. Franz, Georg von Freymann, Martin Wegener, and Martin Bastmeyer. Elastic fully three-dimensional microstructure scaffolds for cell force measurements. *Advanced materials (Deerfield Beach, Fla.)*, 22(8):868–871, 2010.
- [5] Zhen-Lin Wu, Ya-Nan Qi, Xiao-Jie Yin, Xin Yang, Chang-Ming Chen, Jing-Ying Yu, Jia-Chen Yu, Yu-Meng Lin, Fang Hui, Peng-Li Liu, Yu-Xin Liang, Yang Zhang, and Ming-Shan Zhao. Polymer-based device fabrication and applications using direct laser writing technology. *Polymers*, 11(3), 2019.
- [6] Landon Ivy and Amit Lal. Solderable multisided metal patterns enables 3d integrable direct laser written polymer mems. In *2023 35th International Conference on Microelectronic Test Structure (ICMTS)*, pages 1–6, Piscataway, NJ, 2023. IEEE.

- [7] Simone Pagliano, David E. Marschner, Damien Maillard, Nils Ehrmann, Göran Stemme, Stefan Braun, Luis Guillermo Villanueva, and Frank Niklaus. A 3d-printed functional mems accelerometer. In *2023 IEEE 36th International Conference on Micro Electro Mechanical Systems Conference (MEMS)*, pages 594–597, Piscataway, NJ, 2023. IEEE.
- [8] Chun Xia, Edgar Bustamante, Stephen M. Kuebler, Noel P. Martinez, Raymond C. Rumpf, and Jimmy E. Touma. Binary-lens-embedded photonic crystals. *Optics letters*, 47(12):2943–2946, 2022.
- [9] Victoria Paige Stinson, Serang Park, Micheal McLamb, Glenn Boreman, and Tino Hofmann. Photonic crystals with a defect fabricated by two-photon polymerization for the infrared spectral range. *Optics*, 2(4):284–291, 2021.
- [10] Ada-Ioana Bunea, Einstom Engay, Alexandre Emmanuel Wetzel, and Rafael Taboryski. Microswimmers for biomedical applications: Focus on light. In *The 1st International Conference on Micromachines and Applications*, page 8, Basel Switzerland. MDPI.
- [11] Vahid Ebrahiminejad and Zahra Faraji Rad. Design, development, and testing of polymeric microblades: A novel design of microneedles for biomedical applications. *Advanced Materials Interfaces*, 9(29), 2022.
- [12] Koen Vanmol, Ahmed Kandeel, Gebirie Y. Belay, Hugo Thienpont, Heidi Ottevaere, and Jurgen van Erps. Two-photon polymerization-based direct laser writing and characterization of micro-lenses for optical interconnect applications. In *The Twenty-sixth Microoptics Conference*, pages 1–2, Piscataway, NJ, 2021. IEEE.
- [13] Jiawen Li, Simon Thiele, Rodney W. Kirk, Bryden C. Quirk, Ayla Hoogendoorn, Yung Chih Chen, Karlheinz Peter, Stephen J. Nicholls,

- 
- Johan W. Verjans, Peter J. Psaltis, Christina Bursill, Alois M. Herkommer, Harald Giessen, and Robert A. McLaughlin. 3d-printed micro lens-in-lens for in vivo multimodal microendoscopy. *Small (Weinheim an der Bergstrasse, Germany)*, 18(17):e2107032, 2022.
- [14] Maria Göppert-Mayer. Über elementarakte mit zwei quantensprüngen. *Annalen der Physik*, 401(3):273–294, 1931.
- [15] W. Kaiser and C. G. B. Garrett. Two-photon excitation in  $\text{CaF}_2 : \text{Eu}^{2+}$ . *Physical Review Letters*, 7(6):229–231, 1961.
- [16] Joachim Fischer. *Three-dimensional optical lithography beyond the diffraction limit*. Phd thesis, Karlsruher Institut für Technologie, Karlsruhe, 2012.
- [17] Nanoguide: <https://support.nanoscribe.com/hc/en-gb>, 06.08.2023.
- [18] Miłosz Pawlicki, Hazel A. Collins, Robert G. Denning, and Harry L. Anderson. Zweiphotonenabsorption und das design von zweiphotonenfarbstoffen. *Angewandte Chemie*, 121(18):3292–3316, 2009.
- [19] Mariacristina Rumi, Stephen Barlow, Jing Wang, Joseph W. Perry, and Seth R. Marder. Two-photon absorbing materials and two-photon-induced chemistry. In Seth R. Marder, Kwang-Sup Lee, Kwang-söp Yi, and Stephen Barlow, editors, *Photoresponsive polymers*, Advances in polymer science, pages 1–95. Springer, Berlin, 2008.
- [20] Kwang-Sup Lee, Ran Hee Kim, Dong-Yol Yang, and Sang Hu Park. Advances in 3d nano/microfabrication using two-photon initiated polymerization. *Progress in Polymer Science*, 33(6):631–681, 2008.
- [21] Tae Woo Lim, Sang Hu Park, and Dong-Yol Yang. Contour offset algorithm for precise patterning in two-photon polymerization. *Microelectronic Engineering*, 77(3-4):382–388, 2005.

- [22] Xiaoqin Zhou, Yihong Hou, and Jieqiong Lin. A review on the processing accuracy of two-photon polymerization. *AIP Advances*, 5(3), 2015.
- [23] Bidhan Pramanick, Matias Vazquez-Pinon, Alejandro Torres-Castro, Sergio O. Martinez-Chapaa, and Marc Madou. Effect of pyrolysis process parameters on electrical, physical, chemical and electro-chemical properties of su-8-derived carbon structures fabricated using the c-mems process. *Materials Today Proceedings*, 5(3):9669–9682, 2018.
- [24] Qing Sun, Christian Dolle, Chantal Kurpiers, Kristian Kraft, Monsur Islam, Ruth Schwaiger, Peter Gumbsch, and Yolita M. Eggeler. In situ pyrolysis of 3d printed building blocks for functional nanoscale metamaterials. *Advanced Functional Materials*, 2023.
- [25] Joshua B. Tyler, Gabriel L. Smith, Asher C. Leff, Peter M. Wilson, John Cumings, and Nathan Lazarus. Understanding the electrical behavior of pyrolyzed three-dimensional-printed microdevices. *Advanced Engineering Materials*, 23(1), 2021.
- [26] Jens Bauer, Lucas R. Meza, Tobias A. Schaedler, Ruth Schwaiger, Xiaoyu Zheng, and Lorenzo Valdevit. Nanolattices: An emerging class of mechanical metamaterials. *Advanced materials (Deerfield Beach, Fla.)*, 29(40), 2017.
- [27] Ori Stein, Ying Liu, J. Streit, R. Cahayag, Y. Lu, and N. Petta. Handling and assembling of low-density foam structures fabricated by two-photon polymerization. In Eva M. Campo, Elizabeth A. Dobisz, and Louay A. Eldada, editors, *Nanoengineering: Fabrication, Properties, Optics, and Devices XIV*, Proceedings of SPIE, page 20, Bellingham, Washington, USA, 2017. SPIE.



- [28] Andresa Baptista, Francisco Silva, Jacobo Porteiro, José Míguez, and Gustavo Pinto. Sputtering physical vapour deposition (pvd) coatings: A critical review on process improvement and market trend demands. *Coatings*, 8(11):402, 2018.
- [29] Gustavo Pinto, Francisco Silva, Jacobo Porteiro, José Míguez, and Andresa Baptista. Numerical simulation applied to pvd reactors: An overview. *Coatings*, 8(11):410, 2018.
- [30] Jain Neelesh, Sawant Mayur, Nikam Sagar, and Jhavar Suyog. Metal deposition: Plasma-based processes. *Encyclopedia of Plasma Technology*, pages 722–740, 2016.
- [31] André Anders. A structure zone diagram including plasma-based deposition and ion etching. *Thin Solid Films*, 518(15):4087–4090, 2010.
- [32] C. A. Volkert and A. M. Minor. Focused ion beam microscopy and micromachining. *MRS Bulletin*, 32(5):389–399, 2007.
- [33] Jacques Gierak. Focused ion beam nano-patterning from traditional applications to single ion implantation perspectives. *Nanofabrication*, 1(1), 2014.
- [34] Leon van Kouwen. Introduction to focused ion beams, ion sources, and the nano-aperture ion source. In Peter W. Hawkes and Martin Hÿtch, editors, *Including CPO-10*, volume 212 of *Advances in Imaging and Electron Physics*, pages 181–216. Academic Press, London, 2019.
- [35] Shida Tan, Richard Livengood, Darryl Shima, John Notte, and Shawn McVey. Gas field ion source and liquid metal ion source charged particle material interaction study for semiconductor nanomachining applications. *Journal of Vacuum Science & Technology B, Nanotechnology and*

- 
- Microelectronics: Materials, Processing, Measurement, and Phenomena*, 28(6):C6F15–C6F21, 2010.
- [36] M. Knoll and E. Ruska. Das elektronenmikroskop. *Zeitschrift fr Physik*, 78(5-6):318–339, 1932.
- [37] J. R. Jinschek. Advances in the environmental transmission electron microscope (etem) for nanoscale in situ studies of gas-solid interactions. *Chemical communications (Cambridge, England)*, 50(21):2696–2706, 2014.
- [38] Rajaprakash Ramachandramoorthy, Rodrigo Bernal, and Horacio D. Espinosa. Pushing the envelope of in situ transmission electron microscopy. *ACS nano*, 9(5):4675–4685, 2015.
- [39] C. Gammer, J. Kacher, C. Czarnik, O. L. Warren, J. Ciston, and A. M. Minor. Local and transient nanoscale strain mapping during in situ deformation. *Applied Physics Letters*, 109(8), 2016.
- [40] Zaoli Zhang and Dangsheng Su. Behaviour of tem metal grids during in-situ heating experiments. *Ultramicroscopy*, 109(6):766–774, 2009.
- [41] Huolin L. Xin, Kaiyang Niu, Daan Hein Alsem, and Haimei Zheng. In situ tem study of catalytic nanoparticle reactions in atmospheric pressure gas environment. *Microscopy and microanalysis : the official journal of Microscopy Society of America, Microbeam Analysis Society, Microscopical Society of Canada*, 19(6):1558–1568, 2013.
- [42] Chao Zhang, Konstantin L. Firestein, Joseph F. S. Fernando, Dumindu Siriwardena, Joel E. von Treifeldt, and Dmitri Golberg. Recent progress of in situ transmission electron microscopy for energy materials. *Advanced materials (Deerfield Beach, Fla.)*, 32(18):e1904094, 2020.

- [43] Autodesk: <https://www.autodesk.de/>, 04.08.2023.
- [44] Thingiverse: <https://www.thingiverse.com/>, 23.08.2023.
- [45] Korvus technology: <https://korvustech.com/>, 07.09.2023.
- [46] Bruker corporation: <https://www.bruker.com/en/products-and-solutions/test-and-measurement/nanomechanical-instruments-for-semester/push-to-pull-device.html>, 10.01.2024.
- [47] Jens Bauer, Almut Schroer, Ruth Schwaiger, Iwiza Tesari, Christian Lange, Lorenzo Valdevit, and Oliver Kraft. Push-to-pull tensile testing of ultra-strong nanoscale ceramic-polymer composites made by additive manufacturing. *Extreme Mechanics Letters*, 3:105–112, 2015.
- [48] David R. Cayll, Ian S. Ladner, Joon Hyong Cho, Sourabh K. Saha, and Michael A. Cullinan. A mems dynamic mechanical analyzer for in situ viscoelastic characterization of 3d printed nanostructures. *Journal of Micromechanics and Microengineering*, 30(7):075008, 2020.